REPORT DOCUMENTATION PAGE

ERO Proposal Number : R & D # 6148-MS-01 Contract Number : DAJA45-90-C-0052

Title of proposal : Experimental Investigation of Adiabatic Shear Banding at Different Impact Velocities

Repor Number : 05   Period covered : Nov. 1990 - Jan . 1993

Final Technical Report

Name of Institution :

Laboratory of Physics and Mechanics of Materials

URA - CNRS N° 1215

Institut of Applied Mechanics and Technology

Metz University

F-57045 METZ. France

Principal Investigator : J.R. KLEPACZKO

DTIC QUALITY INSPECTED 3

Accession For	
NTIS GRA&I	☑
DTIC TAB	☐
Unannounced	☐
Justification	
By	
Distribution/	
Availability Codes	
Dist	Avail and/or Special
A-1	

Approved for Public Release ; distribution unlimited.

Abstract

In order to expand shear testing to different nominal strain rates a new experimental technique has been developed in the Laboratory of Physics and Mechanics of Materials, Metz, France (LPMM). A modified specimen geometry of double shear has been designed (MDS specimen). The MDS specimen with flat faces is loaded directly by a bar projectile which can be accelerated to a desired impact velocity by a gas gun (1 m/s $\leq V_o \leq 200$ m/s), where V_o is the impact velocity. Since the specimen is backed by a long tube which transmits the force imposed on the MDS specimen the shear stress history can be exactly recorded by the transmitted elastic longitudinal wave. The shear displacement of the MDS specimen is measured directly by an optical gage. The experimental setup which consists of the air gun, transmitter tube (Hopkinson tube) and optical displacement gage, permits for a wide variation of the nominal strain rates, typically 10^2 s^{-1} $\leq \Gamma \leq 10^5$ s^{-1}. On the other hand there is no limitation of maximum shear strain.

The MDS specimen geometry has been calibrated with the FEM and "ABACUS" software.

Evaluation of dispersive effects of elastic longitudinal waves in tubes has been studied, see Appendix n° 2 to the Report. A closed-form solution has been obtained for a semi-infinite tube loaded at the end by the step pressure function $p = p_o H (t)$, where p_o is the amplitude of pressure and $H (t)$ is the Havyside function. Dispersion effects in the real configuration of the MDS specimen and Hopkinson tube have been analysed for several idealised trapezoidal incident pulses using a dynamic FE code. Those calculations revealed characteristic features in dispersive changes of the transmitted pulses by the MDS specimen.

Adiabatic shear banding leads directly to dynamic fracture in Mode II. Because the stress concentrators are present in every loading configuration this causes that the dynamic Mode II is the final stage of the ASB's. A large study of rate effects in Mode II fracture has been performed, Appendix n° 1 to the Report.

The new experimental technique has been applied, as an preliminary stage, to test an annealed low alloy mild steel (0.17% C. 0.58% Mn). It was attempted to find conditions for catastrophic adiabatic shear as a function of impact velocity, up to 100 m/s. An energy analysis have shown that in excess of certain impact velocity, typically for this steel $V_o = 90$ m/s, the energy to break MDS specimen diminishes when the impact velocity is increased. In addition, scanning micrographs were taken of the fracture surfaces.

The second series of experiments have been performed on quenched and tempered VAR 4340 steel. Again, the threshold of impact velocity has been found for this steel in excess of which the critical force, or energy of fracturing, diminishes when impact velocity is increased. The critical impact velocity is estimated as $V_o = 150$ m/s. Scanning electron microscopy revealed characteristic patterns on the fracture surfaces indicating very high temperatures.

CONTENTS

Appendixes*

---

* All Appendixes are under separate covers.

Extended abstract

Since adiabatic shear bands (ASB's) are frequently observed in steels under high rate of deformation, and they are the dominant mode of failure in steels, the interest of studying them is still actual. Although the ASB's have been previously studied, the effect of the nominal strain rate as well as the effects of different impact velocities on ASB's development are not throughly understood.

A commonly used experimental technique in studying the ASB's is the Split Hopkinson Torsion Bar. This technique, although quite effective and precise, has one disadvantage that the nominal rates of shearing are quite limited, typically, $500 \ s^{-1} \leq \dot{\Gamma} \leq 2000 \ s^{-1}$, where $\dot{\Gamma}$ is the rate of shear deformation. In order to expand shear testing to different nominal strain rates a new experimental technique has been developed in the Laboratory of Physics and Mechanics of Materials, Metz, France (LPMM). A modified specimen geometry of double shear has been designed (MDS specimen). The MDS specimen with flat faces is loaded directly by a bar projectile which can be accelerated to a desired impact velocity by a gas gun ($1 \ m/s \leq V_o \leq 200 \ m/s$), where V_o is the impact velocity. Since the specimen is backed by a long tube which transmits the force imposed on the MDS specimen the shear stress history can be exactly recorded by the transmitted elastic longitudinal wave. The shear displacement of the MDS specimen is measured directly by an optical gage. The experimental setup which consists of the air gun, transmitter tube (Hopkinson tube) and optical displacement gage / extensometer, permits for a wide variation of the nominal strain rates, typically $10^2 \ s^{-1} \leq \dot{\Gamma} \leq 10^5 \ s^{-1}$. On the other hand there is no limitation of maximum shear strain.

Since the technique is new preliminary studies have been undertaken to understand better the mechanics of the test.

The MDS specimen geometry has been calibrated with the FEM and "ABACUS" software (O. Oussouaddi).

Evaluation of dispersive effects of elastic longitudinal waves in tubes has been studied (J.R. Klepaczko and S.J. Matysiak), see Appendix n° 2 to the Final Technical Report. A closed-form solution has been obtained for a semi-infinite tube loaded at the end by the step pressure function $p = p_o \ H \ (t)$, where p_o is the amplitude of pressure and H (t) is the Havyside function.

Dispersion effects in the real configuration of the MDS specimen and Hopkinson tube have been analysed for several idealised trapezoidal incident pulses using a dynamic FE code. Those calculations revealed characteristic features in dispersive changes of the transmitted pulses by the MDS specimen.

Adiabatic shear banding leads directly to dynamic fracture in Mode II. Because the stress concentrators are present in every loading configuration and this causes that the dynamic Mode II is the final stage of the ASB's. A large study of rate effects in Mode II fracture has been performed (I.V. Varfolomeyer and J.R. Klepaczko), see Appendix n° 1 to the Final Technical Report.

Different crack geometries in Mode II has been analysed, and some of them can be used with the new experimental setup.

The new experimental technique has been applied, as an preliminary stage, to test annealed low alloy mild steel (0.17% C, 0.58% Mn). It was attempted to find conditions for catastrophic adiabatic shear as a function of impact velocity, up to 100 m/s. An energy analysis have shown that in excess of certain impact velocity, or nominal strain rate, typically for this steel $\dot{\Gamma} = 1.15 * 10^4$ s^{-1}, the energy to break MDS specimen diminishes when the impact velocity is increased. In addition, scanning micrographs were taken of the fracture surfaces.

The second series of experiments have been performed on quenched and tempered VAR 4340 steel. Again, the threshold strain rate has been found for this steel in excess of which the critical force, or energy of fracturing, diminishes when impact velocity is increased. The threshold strain rate is estimated as $\dot{\Gamma} = 10^5$ s^{-1}. Scanning electron microscopy revealed characteristic patterns on the fracture surfaces indicating very high temperatures.

Although the new experimental technique needs further improvements it appeared to be useful and effective.

List of Keywords :   Steel
                       1018 steel
                       4340 steel
                       High strength alloys
                       Shear tests
                       Adiabatic shear bands
                       Fracture

Introduction

During last decade a substantial progress has been made in testing, analytical solutions and numerical calculations of the Adiabatic Shear Bands. It is well known for a long time, for example, the paper by H. Tresca (1878) [1], and revue by W. Johnson (1987) [2], of early works, that metals can develop a thermal instability of plastic flow due to heat generated during deformation. Zener and Hollomon (1944) [3], noted that an increase strain rate is inevitably associated with a change of deformation conditions from isothermal to adiabatic. The same authors found that the plastic deformation becomes unstable when the strain hardening rate (the tangent modulus of the stress-strain curve) starts to be negative. Although localisation of plastic deformation in the form of shear bands is very common in many materials, a great deal of interest has been recently devoted to study the non-isothermal cases. The present study is also limited to the non-isothermal case when the adiabatic conditions of plastic deformation prevail.

At moderately high and high strain rates plastic deformation in metals is nearly adiabatic, as a consequence the deformation heating can lead to sizeable amount of flow softening and hence to flow localization in the form of ASB, called also the thermoplastic catastrophic shear, which can inturn lead to fracture. The ASB's are narrow, a small fraction of millimeter, zones of highly non-homogeneous deformation developed by a complicated interplay of strain hardening, temperature softening, strain rate sensitivity, dynamic strain ageing and sometimes inertia forces. In some materials, specially in steels and titanium alloys, a phase transformation or amorphous-like microstructure may develop within a narrow zone of the highest temperatures. It may be mentioned that there is no agreement as to a state of structure inside the ASB's for different materials. It may be mentioned also that ASB's, with or without phase transformation, often act as sites of fracture initiation in Mode II, [4]. The importance of the ASB's is obvious in diverse applications like rolling, drawing, machining, impact on structures and ballistic impact.

A number of analytical, numerical and experimental studies have been performed in attempt to determine the critical conditions for the onset and evolution of catastrophic thermoplastic shear. The early revues on the subject demonstrated difficulties in the analysis of the problem, for example [5]. A more recent up-to-date review was published by Bai and Dodd, [6].

Analytical studies of ASB are more numerous and they will not be reviewed in this Report. Generally, because of simplicity of constitutive relations, in order to find a closed form solution, inacceptable simplifications were automatically introduced in some ASB analyses. More recent analytic studies are more acceptable, for example [7-10].

On the other hand, more and more numerical analyses on ASB formation are available, and in general, the final results are very sensitive to constitutive relations chosen. Although very frequently the fully non-linear system of equations is employed in such studies, the material behavior characterized in the form of constitutive relations is quite simplified. Such situation may lead to

Introduction

During last decade a substantial progress has been made in testing, analytical solutions and numerical calculations of the Adiabatic Shear Bands. It is well known for a long time, for example, the paper by H. Tresca (1878) [1], and revue by W. Johnson (1987) [2], of early works, that metals can develop a thermal instability of plastic flow due to heat generated during deformation. Zener and Hollomon (1944) [3], noted that an increase strain rate is inevitably associated with a change of deformation conditions from isothermal to adiabatic. The same authors found that the plastic deformation becomes unstable when the strain hardening rate (the tangent modulus of the stress-strain curve) starts to be negative. Although localisation of plastic deformation in the form of shear bands is very common in many materials, a great deal of interest has been recently devoted to study the non-isothermal cases. The present study is also limited to the non-isothermal case when the adiabatic conditions of plastic deformation prevail.

At moderately high and high strain rates plastic deformation in metals is nearly adiabatic, as a consequence the deformation heating can lead to sizeable amount of flow softening and hence to flow localization in the iorm of ASB, called also the thermoplastic catastrophic shear, which can inturn lead to fracture. The ASB's are narrow, a small fraction of millimeter, zones of highly non homogeneous deformation leveloped by a complicated interplay of strain hardening, temperature softening, strain rate sensitivity, dynamic strain ageing and sometimes inertia forces. In some materials, specially in steels and titanium alloys, a phase transformation or amorphous-like microstructure may develop within a narrow zone of the highest temperatures. It may be mentioned that there is no agreement as to a state of structure inside the ASB's for different materials. It may be mentioned also that ASB's, with or without phase transformation, often act as sites of fracture initiation in Mode II. [4]. The importance of the ASB's is obvious in diverse applications like rolling, drawing, machining, impact on structures and ballistic impact.

A number of analytical, numerical and experimental studies have been performed in attempt to determine the critical conditions for the onset and evolution of catastrophic thermoplastic shear. The early revues on the subject demonstrated difficulties in the analysis of the problem, for example [5]. A more recent up-to-date review was published by Bai and Dodd, [6].

Analytical studies of ASB are more numerous and they will not be reviewed in this Report. Generally, because of simplicity of constitutive relations, in order to find a closed form solution, inacceptable simplifications were automatically introduced in some ASB analyses. More recent analytic studies are more acceptable, for example [7-10].

On the other hand, more and more numerical analyses on ASB formation are available, and in general, the final results are very sensitive to constitutive relations chosen. Although very frequently the fully non-linear system of equations is employed in such studies, the material behavior characterized in the form of constitutive relations is quite simplified. Such situation may lead to

some misinterpretations of how ASB's evolve as a function of both the initial and boundary conditions.

The state of the art is that relatively large quantity of theoretical studies have been so far published with much less effort put into experiment. Most of experimental studies make use of Split Hopkinson Torsion Bar (torsional Kolsky apparatus), [11-13]. They are based on fast torsion of thin tubular specimens of short lengths. Such test with SHTB has a very limited range (in the logarithmic scale) of the nominal shear strain rates, usually around 10^3 s^{-1}, and the boundary conditions imposed during the test, although well defined, are not constant, [14]. Thus, majority of experimental studies were limited to a thin tubular geometry and to the nominal strain rates around 10^3 s^{-1}. The other range of rates, albeit much higher, is met in external ballistics and explosive loading. Although it is very easy to produce a network of ASB's during ballistic or explosive loadings, they do not provide a good experimental basis to study fundamentals.

The most important, and so far unresolved class of problems, is the effect of initial and boundary conditions on the onset and formation of the ASB's. From the point of view of experiments the following loading schemes can be specified :

i. Initially uniform deformation field with small initial perturbations :

   the initial perturbations which are usually assumed :

      a. small defect of geometry :

      b. small thermal perturbations :

      c. heat sinks.

ii. Imposed deformation fields with instantaneous stress or strain concentrators :

      a. controlled loading conditions :

      b. direct impact at different velocities (including ballistic impact) and different projectile/target geometries.

iii. Explosive loading :

      a. expansion of tubes (fragmentation via ASB's) :

      b. shock waves generated on limited surfaces.

iv. Controlled shock waves :

      a. plate/plate impact (micro ASB's).

v. Metal forming processes :

      a. machining :

      b. high speed rolling :

      c. high speed drawing.

The systematics shown above points out on a wide class of loading conditions, and in turn, on a wide class of initial and boundary conditions under which the ASB's can be generated. The cases iii., iv. and v. will not be discussed here, however, the most fundamental cases, i. and ii., are worth of discussion. The case i. is clearly related to SHTB technique. It can be point out that the active specimen length and initial conditions can influence the outcome in the form of ASB. For

example Litonski [15] has furnished a detailed analysis of the deformation in torsion of a thin-walled tube with an initial geometric imperfection in the form of a slightly thinned section. The analysis was repeated in a similar way by Costin et al. [11] but with comparison to SHTB experiments on 1018 CRS (cold rolled steel) and 1020 HRS (hot rolled steel). Sometime later Litonski [16] have shown by a similar numerical analysis, but the thin-walled tube without geometric imperfection has been analysed and with the heat sinks at the ends, that the ASB occurs above certain critical strain rate of the order $1.0\ s^{-1}$. Another numerical study was reported in [17] where a thin-walled tube of a constant cross-section had a Gaussian imperfec-tion of the yield stress τ_y, i.e. $\tau_y(x) = \tau_{yo}\ G(x)$, where $G(x)$ is the Gaussian distribution and τ_{yo} is the mean yield stress. It was shown in this study that at lower nominal strain rates, of the order $0.1\ s^{-1}$, the strain and temperature fields differ for the adiabatic and heat conduction cases. When the nominal strain rate was increased to $1\ s^{-1}$ the differences were substantially reduced.

Also later the geometry imperfections were the most frequently studied cases. In [18] are reported numerical simulations of ASB's observed on 1020 in [11]. Plastic instability and flow localization in shear at high rates of deformation were studied in [19] by assuming a geometrical imperfection in specimen. In [20] the effects of material imperfections via geometric imperfections on flow localization in SHTB test were studied.

Shawki and Clifton. [21] presented a number of analytic solutions and numerical studies, including torsion of a thin tube with geometrical imperfections, with one or more circumferential grooves and with thermally isolated sides. Three simple constitutive relations were used in those calculations. It was found, as expected, that at high nominal strain rates of the order 10^3 to $10^4\ s^{-1}$ the localization mechanism which accounts for ASB formation is exclusively adiabatic. For this mechanism, at advanced deformation the thermal softening dominates in reduction of stress and an increase of local shear strain leading to catastrophic local shearing. At small strains a positive strain hardening dominates and localization does not occur. The rate of localization depends strongly on the strain rate sensitivity. The qualitative discussion as offered above is consistent with earlier findings and physical intuition. The qualitative analyses of the ASB's formation for particular metals and alloys and for different boundary conditions are still waiting to be solved.

A more recent numerical study, [22] have shown that the heat sinks introduced at the ends of a thin-walled tube can modify the whole process of the ASB formation in comparison to the assumption of the adiabatic boundary conditions. In addition to the heat sinks a temperature perturbation was introduced. A small local maximum in the initial temperature distribution along the tube axis developed formation of the ASB just in this cross section. A simple linear Arrhenius model combined with a power strain hardening was employed in those calculations, the nominal strain rate was assumed as $1.6 \times 10^3\ s^{-1}$. Again, numerical results discussed above clearly indicate the importance of the initial and boundary conditions on final geometry and formation of the ASB's.

Transition from isothermal to adiabatic deformation

The localization of deformation in the form of ASB's is observed in thin-walled tubes when the nominal strain rate exceeds certain value. Obviously, a transition exists between pure isothermal and pure adiabatic regimes of deformation. This transition depends in the first place on geometry of deformed body and on effectiveness of heat evacuation from the heat zones. When correct boundary and initial problems are posed it is possible to estimate the range of strain rates within which the transition occurs. Preliminary calculations to find an approximate strain rate range of transition were reported in [15] and [17]. In the second case numerical calculations were performed for the length of tube L = 30 mm and initial temperature 673K, and three cases were studied : isothermal, adiabatic and mixed, when it was allowed for heat conduction. Three nominal strain rates were assumed : 0.01 ; 0.1 and 1.0 s^{-1}. The final results of those calculations have shown that the difference between adiabatic and mixed cases is substantially reduced for shear strain rate 1.0 s^{-1}. A similar calculation was performed in [16] for a thin-walled tube, L = 5.0 mm, and with the heat sinks at the ends, again the initial temperature was assumed T_0 = 673K, and four values of nominal strain rates were considered : 0.01 ; 0.1 ; 1.0 and 10.0 s^{-1}. Similar plots were produced for the complete case (heat conduction included). It was found that the transition must occur between nominal strain rates 0.1 and 1 s^{-1}.

A more exact transition analysis for thin-walled tubes of different lengths was performed more recently by Oussouaddi and Klepaczko [23]. The finite difference technique has been applied with relatively exact constitutive relation, and calculations were carried out at different nominal strain rates in shear from 1.0 s^{-1} to 10^3 s^{-1}, at T_0 = 300K. In addition, the effect of length on the isothermal/ adiabatic transition was studied. Since the heat sinks were assumed at the tube ends the transition was defined as the maximum of partial derivative of the temperature gradient with respect to the nominal strain rate $\dot{\Gamma}_n$

$$\xi = \frac{\partial}{\partial \log \dot{\Gamma}_n} \left(\frac{\partial T}{\partial x} \right)$$

(1)

where x is the axial coordinate : $- L/2 \leq x \leq L/2$, T is the absolute temperature and $\dot{\Gamma}_n = d\Gamma_n/dt$ is the nominal strain rate in shear, $\Gamma_n = (r/L)\, \varphi$, r is the mean radius and φ the angle of twist. The temperature gradients as a function of log $\dot{\Gamma}_n$ for L = 2.0 mm are shown in Fig. 1a, whereas Fig. 1b shows variation of ξ also as a function of log $\dot{\Gamma}_n$. It is clear that the transition can be well defined by the maximum value of ξ. The critical values of $(\dot{\Gamma}_n)_{cr}$ are given in Table 1, and also shown in Fig. 2 as a function of L. The results support qualitatively the physical intuition that the critical strain rate increases in proportion to the thermal conductivity, which is the lowest for steel and the highest for copper. When L decreases from 10 mm to 1.0 mm the critical strain rate increases approximately twofold for all three material which were studied.

Those results clearly indicate the importance of the boundary and initial conditions, in both experiment and numerics, not only in the case of transition isothermal/adiabatic, but also in formation of ASB's.

Table 1

Critical shear strain rate (s^{-1})

Length (mm)	Steel	Aluminium	Copper
1	58.8	89.0	112.0
2	47.5	68.5	84.5
4	40.5	54.0	66.0
6	36.0	50.0	59.0
10	31.0	42.0	49.0

Shear strain of instability

The earliest studies on the onset of the shear localization were limited, by analogy to Considère condition of instability in tension test, to the load instability $dM/d\varphi = 0$. The condition $dM/d\varphi = 0$, where M is the torque and φ is the angle of twist, gives possibility to determine the critical instability strain if a specific constitutive relation is assumed. It was confirmed by Litonski [15], by numerical application of the flow localization model (Marciniak-Kuczynski approach [24]), that the onset of instability corresponds to the maximum load, that is the condition $dM/d\varphi = 0$ was confirmed as the onset of instability. Many authors derived formulas for the critical strain using different empirical constitutive relations, a review of those derivations was published in [25]. Experimental confirmation of the onset condition $dM/d\varphi = 0$ was provided for a low-alloy structural steel in [13]. A high speed photography combined with SHTB technique was applied in those study.

Since up to the maximum of torque the shear deformation is uniform the condition for load instability reduces to the formula

$$\frac{d\tau}{d\Gamma} = 0 \tag{2}$$

Because many authors use constitutive relations in the form of multiplication function

$$\tau = f_1(T) f_2(\Gamma) f_3(\dot{\Gamma}) \tag{3}$$

a more general analysis of the condition (2) will be given, Klepaczko, [26]. If the mechanical equation of state is assumed and the history effects are neglected one can write

$$\frac{d\tau}{d\Gamma} = \left(\frac{\partial\tau}{\partial\Gamma}\right)_{T,\dot\Gamma} + \left(\frac{\partial\tau}{\partial T}\right)_{\Gamma,\dot\Gamma}\frac{dT}{d\Gamma} + \left(\frac{\partial\tau}{\partial\dot\Gamma}\right)_{T,\Gamma}\frac{d\dot\Gamma}{d\Gamma} \tag{4}$$

then the condition (2) leads to

$$\left(\frac{\partial\tau}{\partial\Gamma}\right)_{T,\dot\Gamma} + \left(\frac{\partial\tau}{\partial T}\right)_{\Gamma,\dot\Gamma}\frac{dT}{d\Gamma} + \left(\frac{\partial\tau}{\partial\dot\Gamma}\right)_{T,\dot\Gamma}\frac{d\dot\Gamma}{d\Gamma} = 0 \tag{5}$$

Condition (5) can be satisfied only in very specific conditions of deformation. One of them is the adiabatic process of deformation, then

$$\frac{dT}{d\Gamma} = \left(\frac{dT}{d\Gamma}\right)_{ADIABATIC} \tag{6}$$

Condition (5) can be analysed for variety of deformation histories $\dot\Gamma(\Gamma)$ and $T(\Gamma)$, but the simplest case is usually limited to the constant strain rate, in general

$$\left(\frac{\partial\tau}{\partial\Gamma}\right)_T - \left(\frac{\partial\tau}{\partial T}\right)_\Gamma \left(\frac{dT}{d\Gamma}\right)_A = 0 \tag{7}$$

It is important, then, to have an estimate of the adiabatic increase of temperature $T_A(\Gamma)$ and $(\partial T/d\Gamma)_A$ due to plastic work converted into heat. Assuming constitutive relation (2) it follows from the principle of energy conservation

$$\left(\frac{dT}{d\Gamma}\right)_A = \frac{[1 - \zeta(T,\Gamma)]\,f_1(T)\,f_2(\Gamma)\,f_3(\dot\Gamma)}{\rho(T)\,C_p(T)} \tag{8}$$

where $\zeta(T,\Gamma)$ is a coefficient taking into account the stored energy in the material, $\rho(T)$ is the mass density of the material and $C_p(T)$ is the specific heat at constant pressure, both ρ and C_p are function of temperature.

The partial differentials can be found after (3) as follows

$$\left(\frac{\partial\tau}{\partial T}\right)_{\Gamma,\dot\Gamma} = f_2(\Gamma)\,f_3(\dot\Gamma)\frac{\partial f_1}{\partial T}$$

$$\left(\frac{\partial\tau}{\partial\Gamma}\right)_{\dot\Gamma,T} = f_1(T)\,f_3(\dot\Gamma)\frac{\partial f_2}{\partial\Gamma}$$

$$\left(\frac{\partial\tau}{\partial\dot\Gamma}\right)_{\Gamma,T} = f_1(T)\,f_2(\Gamma)\frac{\partial f_3}{\partial\dot\Gamma} \tag{9}$$

Introduction (9) into condition (4) yields

$$\frac{1}{f_2(\Gamma_c)}\left(\frac{\partial f_2}{\partial\Gamma}\right) + \frac{1}{f_1(T)}\left(\frac{\partial f_1}{\partial T}\right)\left(\frac{dT}{d\Gamma}\right)_A + \frac{1}{f_3(\dot\Gamma)}\left(\frac{\partial f_3}{\partial\Gamma}\right) = 0 \tag{10}$$

After elimination of $(dT/d\Gamma)_A$ using (8) the condition (10) is transformed into the following form

$$\frac{1}{f_2(\Gamma_c)}\left(\frac{\partial f_2}{\partial \Gamma}\right) + f_2(\Gamma_c) f_3(\dot{\Gamma})\left(\frac{\partial f_1}{\partial T}\right) \frac{1-\xi}{\rho(T)C_p(T)} + \frac{1}{f_3(\dot{\Gamma})}\left(\frac{\partial f_3}{\partial \Gamma}\right)\left(\frac{d\dot{\Gamma}}{d\Gamma}\right) = 0 \tag{11}$$

where Γ_c is the strain at the onset of instability.

If the strain rate is constant, $(d\dot{\Gamma}/d\Gamma) = 0$, condition (11) reduces to

$$\frac{\partial f_2}{\partial \Gamma} + f_2^2(\Gamma_c) f_3(\dot{\Gamma})\left(\frac{\partial f_1}{\partial T}\right) \frac{1-\zeta}{\rho(T)C_p(T)} = 0 \tag{12}$$

Since only $f_2(\Gamma_c)$ depends on the critical strain the explicit equation for $f_2(\Gamma_c)$ is

$$f_2(\Gamma_c) = \left[-\frac{(\partial f_2/\partial \Gamma)}{(\partial f_1/\partial T)} \frac{\rho(T)C_p(T)}{f_3(\dot{\Gamma})(1-\zeta)}\right]^{1/2} \tag{13}$$

The expression $[-A]^{1/2}$ has real and imaginary part. Inversion of $f_2(\Gamma_c)$ makes it possible to find Γ_c

$$\Gamma_c = f_2^{-1}\left[-A(\Gamma, \dot{\Gamma}, T)\right]^{1/2} \tag{14}$$

where - A is the expression in the square brackets of (13). Existence of the real $f_2(\Gamma_c)$ is possible only if A is negative. Since ρ, C_p, $(1-\xi)$ must be always positive and the function of strain rate sensitivity, $f_3(\dot{\Gamma})$, is assumed in this case also positive, the only term which may be negative is $(\partial f_2/\partial \Gamma)/(\partial f_1/\partial T)$. The most common case is the thermal softening which leads to negative value of $\partial f_1/\partial T$, of course, if $\partial f_2/\partial \Gamma$ is at the same time positive. Another possibility is if the tangent modulus $\partial f_2/\partial \Gamma$ is negative and at the same time there is no thermal softening. The role of a positive rate sensitivity is quite interesting, that is if $f_3(\dot{\Gamma})$ is an increasing function of strain rate $\dot{\Gamma}$. The positive rate sensitivity has a negative effect on the onset of adiabatic instability, that is Γ_c is reduced when strain rate is increased. The positive rate sensitivity increases production of plastic work converted into heat. However, after the critical strain Γ_c is reached, $\Gamma > \Gamma_c$, a positive rate sensitivity diminishes local strain gradients in ASB's. Since the assumption was made $(d\dot{\Gamma}/d\Gamma) = 0$, function $f_3(\dot{\Gamma})$ plays a role of parameter, it must be constant but rate dependent.

In many publications constitutive relations are employed which fall into the class of equation (3). For example, in [15-17] and other publications, the following relation was used in numerical studies

$$\tau = B(1-aT)\left(1 + b\dot{\Gamma}\right)^m \Gamma^n \tag{15}$$

where n is the strain hardening index and m is the rate sensitivity, a, b, B are empirical constants. In this case the thermal softening term has been linearized. Another authors employed the following constitutive relation, for example [7, 9, 21]

$$\tau = B \left(\frac{T_0}{T}\right)^v \left(\frac{\Gamma}{\Gamma_0}\right)^n \left(\frac{\dot{\Gamma}}{\dot{\Gamma}_0}\right)^m$$

(16)

where B, v, n, m are respectively plasticity modulus, temperature index, strain hardening index and logarithmic strain rate sensitivity, T_0, Γ_0 and $\dot{\Gamma}_0$ are normalization constants. Relation (16) falls in the class of non-linear liquids since $\tau = 0$ if $\dot{\Gamma} \rightarrow 0$. This relation was used many times for both, numerical solutions and perturbation analyses, for example [7, 21, 27, 28], and others.

To discuss further the condition of adiabatic instability it is assumed that the flow stress is represented by a more specific relation

$$\tau = B\,(T)\,\Gamma^n\,\dot{\Gamma}^m$$

(17)

where B (T) is known temperature-dependent plasticity modulus. The condition (10) yields the following relation

$$n\,\Gamma_c^{n-1} \div \Gamma_c^n\,\dot{\Gamma}^m \left(\frac{\partial B}{\partial T}\right) \frac{1-\zeta}{\rho_0 C_p(T)}$$

(18)

it is assumed that the mass density ρ_0 and the coefficient of stored energy remain constant. After (18) the critical shear strain at the onset of instability is

$$\Gamma_c = \left[\frac{n\rho_0 C_p(T)}{(1-\zeta)\dot{\Gamma}^m \left(-\frac{\partial B}{\partial T}\right)}\right]^{\frac{1}{n-1}}$$

(19)

A positive role of strain hardening in delaying the adiabatic instability was well documented in early publications. Since the specific heat is an increasing function of temperature it also delays instability. The most important factor is the mathematical form of the $(-\partial B/\partial T)$, especially in the case of post-critical analyses.

Adiabatic increments of temperature at the point of instability, $\partial\tau/\partial\Gamma = 0$, are not usually very high, and constancy of n and m are acceptable. Constant values of n and m are only the first approximation for small increments of temperature. Since it has been shown in [29] and later in [13] that the rise of the post-critical temperature for steels is of the order $425\,K \leq \Delta T \leq 595\,K$ at the central part of the ASB, the constancy of n and m is a very crude approximation. A similar conclusion was reached in [30] by numerical analysis of a thin-walled torsion test specimen. The thermal softening - $(\partial B/\partial T)$ was assumed linear in the first calculations of the post-critical deformation of copper and bilinear in the second one. Substantial differences were revealed in the evolution of stresses in both stages of deformation, up to the instability points and during localization. Another paradox of the temperature-independent logarithmic rate sensitivity, if the thermal softening $(\partial\tau/\partial T)$ is negative, lies in the fact that the stress differences at two constant strain rates increase according to formula (17) when temperature is decreased, this is in complete

contradiction to the real behavior of metals, [31]. A more rational approach is to use some form of Arrhenius relation to take into account at the same time thermal softening and temperature-dependent rate sensitivity, for example [21] and also [22].

Because of complexity in formation of the ASB's the analytic studies in this area, although important, have qualitative character, mostly due to simplistic constitutive relations. The importance must be focused on a full numerical approach with physically-based constitutive relations.

Some results of numerical studies

Among publications on numerical analyses of ASB's only few take into account the fully non-linear system of governing equations. However, the crucial problem, even for the complete formulation, is the choice of constitutive relations.

Two boundary value problems are the most interesting from the point of view of experimental techniques :

i. fast torsion of a thin-walled tube (interesting due to SHTB technique) ;
ii. fast shearing of a layer of finite hight (interesting due to a new experimental technique described in the next part of this report).

Relatively complete analysis of torsion was reported in [22]. Numerical study of a layer as a complete non-linear problem, fully coupled with temperature, was reported in [32]. The fully coupled problem was formulated including heat conduction, changes of specific head as a function of temperature, complete effects of temperature on mechanical properties and inertia. The layer with geometric imperfection was assumed, and the top and bottom of the layer were adiabatically isolated. A complete phenomenological constitutive relation has been used in those calculations. A more exact analysis and discussion of this constitutive relation is published elsewhere, [33]. The fully temperature coupled constitutive relations are as follows

$$\tau = B\,(\theta)\,\left(\Gamma_0 + \Gamma\right)^{n(\theta)} \dot{\Gamma}^{m(\theta)} + <\,\eta\,(\theta)\,\left(\dot{\Gamma} - \dot{\Gamma}_0\right)\,> \tag{20}$$

where θ is the homologous temperature, $\theta = T/T_m$, and T_m is the melting temperature of a material under consideration, η is the pseudo-viscosity and $< \cdot >$ is the operator, $< \cdot > = 0$ if $\dot{\Gamma} \leq \dot{\Gamma}_0$ and $< \cdot > = 1$ if $\dot{\Gamma} > \dot{\Gamma}_0$, $\dot{\Gamma}_0$ is the threshold strain rate. Both, strain hardening index n and logarithmic rate sensitivity m are coupled with temperature. For BPC metals m and n are expressed as a function of θ as follows

$$n\,(\theta) = n_0 \frac{\mu\,(\theta)}{\mu_0} \tag{21}$$

$$m(\theta) = a\,\theta \exp(-b\,\theta) + \alpha_o\,\theta^r \tag{22}$$

where n_o is the strain hardening index at 0K, and a, b, α_o and r are constants, $\mu(\theta)$ is temperature-dependent shear modulus of elasticity

$$\mu(\theta) = \mu_o\left[1 - \theta \exp\left(\theta_\mu\left(1 - \frac{1}{\theta}\right)\right)\right] \tag{23}$$

where μ_o is the shear modulus at 0K and θ_μ is a constant. All constants for two steels (1018 CRS and 1020 HRS) are identified in the paper which was mentioned above. Variation of specific heat was taken into account according to Debye formulation. Geometric imperfection was assumed in the form

$$w(y) = w_o\left\{1 + \delta \sin\left[\pi\left(\frac{1}{\epsilon} - 2\,\epsilon\,\frac{y}{h}\right)\right]\right\} \tag{24}$$

where w_o is the layer thickness and h is the layer height, δ and ϵ are geometry parameters. Equations of momentum, balance of energy with adequate Fourier constant for heat conduction and compatibility condition were assumed in their standard form in those calculations. Numerical calculations were performed using the finite difference implicit method. The duration of the successive time increments were chosen in such a way that the algorithm was unconditionally stable. The boundary conditions were assumed that the bottom surface of the layer was fixed and a constant velocity V was imposed to the top, a steady state process.

The input for those calculations was the nominal strain rate in shear $\dot{\Gamma}_n = V/h$. The output of calculations consisted of a detailed spatial history of all important physical quantities like shear stress $\tau(y,t)$, strain $\Gamma(y,t)$, strain rate $\dot{\Gamma}(y,t)$, absolute temperature $T(y,t)$ and local velocity v (y,t). Thus, the simulation provided a whole dynamic history of the ASB development at different nominal strain rates $\dot{\Gamma}_n$.

Two values of critical nominal strains were evaluated, the instability strain Γ_c associated with the maximum force and the final localization strain Γ_{LOC} defined as follows

$$\Gamma_n \rightarrow \Gamma_{LOC} \quad \text{when} \quad \lim \dot{\Gamma}_B = \infty$$
$$\dot{\Gamma}_A \rightarrow 0 \tag{25}$$

where $\dot{\Gamma}_A$ is the local strain rate in the strongest section of the layer and $\dot{\Gamma}_B$ is the local strain rate in the cross section where localization occurs. Numerical solutions obtained for two steels within the range of nominal strain rates $10^2\ s^{-1} \leq \dot{\Gamma}_n \leq 10^4\ s^{-1}$, (1018 CRS and 1020 HRS) have shown a minimum of both values of $\dot{\Gamma}_n$, i.e Γ_c and Γ_{LOC} at the nominal strain rate $\sim 2\times10^3\ s^{-1}$. Values of Γ_{LOC} were obtained numerically using the condition $\dot{\Gamma}_{LOC} = 10^2\ \dot{\Gamma}_n$. In the range of $\dot{\Gamma}_n$ lower than $\dot{\Gamma}_n = 2\times10^3\ s^{-1}$ both nominal strains Γ^c and Γ_{LOC} decrease when $\dot{\Gamma}_n$ is increased, the trend in accordance to formulas (13) and (19). In the range of the nominal strain rates higher than $\dot{\Gamma}_n = 2\times10^3\ s^{-1}$ a slight increase of Γ_c and Γ_{LOC} is observed. Since calculations were performed twice

withcut pseudo-viscosity, $\eta = 0$, and with pseudo-viscosity the positive effect of excessive strain rate sensitivity on the localization is obvious. The ratio Γ_{LOC}/Γ_c increases at the higher rate if the pseudo-viscosity is included into calculations, if only the logarithmic rate sensitivity is taken into calculations the ratio Γ_{LOC}/Γ_c increases only slightly as a function of $\dot{\Gamma}_n$. It has been, thus, shown in the paper discussed above that for a given material and a given geometric imperfection, there exists a domain of nominal strain rates $\dot{\Gamma}_n$ where development of the catastrophic shear in the form of the ASB is the most likely to occur. A similar minimum of Γ_c was also found in [34] using a finite element technique, and confirmed later in [35] by an approximate method. In both cases the initial temperature defect was assumed. Attempts to find the final thickness of ASB's after numerical results reported in [32] were not quite successful. Although it was found that ASB's were formed the asymptotic width was difficult to estimate since at $\dot{\Gamma}_{LOC} = 10^2\,\dot{\Gamma}_n$ the evolution of ASB's were still not finished. One of reasons why it was difficult to specify a finite thickness of the ASB is the excessive strain hardening introduced by the term $\Gamma^{n(T)}$ at large strains, even when the correct relation for n(T) was used.

As an result a completely new series of numerical calculations were undertaken, but this time a physically based set of constitutive relations have been used. Here only some results will be discussed, a more thorough of that study is given elsewhere, [36]. The constitutive modeling is represented by a consistent approach to the kinetics of macroscopic plastic behavior of metals with BCC and FCC structures, [37, 38]. The constitutive formalism is used here with one state variable which is the total dislocation density ρ. The notion is adopted that plastic deformation in shear is the fundamental mode of deformation. It is assumed that at constant microstructure the flow stress τ has two components : the internal stress τ_μ and the effective stress τ^*, thus

$$\tau = \tau_\mu\Big[h\left(\dot{\Gamma},T\right),\,\dot{\Gamma},\,T\Big]_{STR} + \tau^*\left(\dot{\Gamma},\,T\right)_{STR} \tag{26}$$

where h $(\dot{\Gamma},T)$ are the histories of plastic deformation, Γ and $\dot{\Gamma}$ are respectively plastic strain and strain rate. The internal stress τ_μ is developed by long range strong obstacles to dislocation motion, and the effective stress τ^* is due to thermally activated short range obstacles. In fact, the internal stress τ_μ must be also rate- and temperature-dependent via dynamic recovery or annihilation processes. To describe completely strain rate and temperature effects, including evolution of microstructure and strain hardening, an evolution equation must be defined. In this case a simple evolution equation has been adopted which is adequate to account for strain hardening in mild steels, [37]

$$\frac{d\rho}{d\Gamma} = M_\mathbf{g}\cdot k_\mathbf{a}\left(\dot{\Gamma},T\right)\left(\rho - \rho_q\right) \tag{27}$$

where ρ_o is the initial dislocation density and k_a $(\dot{\Gamma},T)$ is the annihilation factor. The multiplication factor $M_\mathbf{g}$ is related to the mean free path λ of dislocation storage by the formula $M_\mathbf{g} = 1/b\lambda$, where

b is the modulus of Burgers vector. For constant temperature and strain rate the explicit form for ρ can be found after integration of (27)

$$\rho = \rho_0 + \frac{M_{II}}{k_a(\dot{\Gamma},T)}\left[1 - \exp\left(-k_a(\dot{\Gamma},T)\Gamma\right)\right]$$

(28)

If strain rate and temperature are not constant, like in the case of ASB formation, the evolution equation must be numerically integrated to find current value of ρ. If ρ is found the internal stress is also found from the relation

$$\tau_\mu = \alpha\,\mu(T)\,b\,\sqrt{\rho}$$

(29)

where α is dislocation/obstacle interaction constant, and $\mu(T)$, the shear elasticity modulus is specified by eq. (23). Annihilation factor k_a is given by the formulas

$$k_a = k_o \quad \text{for} \quad 0 \leq T \leq T.$$

and

$$k_a = k_o\left(\frac{\dot{\Gamma}_o}{\dot{\Gamma}}\right)^{2m_a(T-T)} \quad \text{for} \quad T. < T < T_m$$

(30)

A constant value for $k_a = k_o$ for $0 \leq T \leq T.$ is a good approximation for mild steels which have an ability to dynamic strain ageing [39]. Equations from (27) to (30) characterize completely evolution of the internal stress τ_μ.

The effective stress τ^* can be deduced from generalised Arrhenius relation, [37, 38]

$$\dot{\Gamma} = v_k(\rho_m,T)\left[\exp - \frac{\Delta G_k(\tau^*,T,\rho_m)}{kT}\right]$$

(31)

where v_k is the frequency factor for the kinetics of double dislocation kink, and ΔG_k is the free energy of activation for this micromechanism. Inversion of eq. (31) leads to the explicit formula for the effective stress

$$\tau^* = \tau_o\left(1 - \left[\frac{kT}{2H_k}\log\left(\frac{v_k}{\dot{\Gamma}}\right)\right]^{1/q}\right)^{1/p}$$

(32)

In this case the universal form for the free energy ΔG_k was employed, [40]

$$\Delta G = G_o\left[1 - \left(\frac{\tau^*}{\tau_o}\right)^p\right]^q$$

(33)

with

$$\tau_o^* = \frac{G_o \sqrt{\rho_m}}{b\, a^*} \quad \text{and} \quad \rho_m = f \rho \tag{34}$$

where G_o is the energy of the double kink formation and τ_o^* is the Peierls stress at 0K, a^* is the activation distance, $a^* = n\, b$, [37, 41]. The frequency factor v_k is assumed in the form

$$v_k = f_o n\, b^2 v_D \rho_o \left[1 + \frac{f_1}{f_o} \exp\left(\frac{T_r}{2T}\right) \log\left(\frac{\rho}{\rho_o}\right) \right] \tag{35}$$

where f_o is the initial fraction, eq. (34), ρ_m is the mobile dislocation density, v_D is Debye frequency, f_1, T_r are constants. The set of equations from (32) to (35) provide complete evolution of the effective stress τ^*.

This constitutive modeling involves two kinds of constants, the absolute physical constants and the constants also based on physics but specified for a particular metal or alloy. The complete discussion of all constants will be given elsewhere, [36], but some basic values are given below : $M_{II} = 1.2 \times 10^{10}$ cm^{-2} ; $T_* = 558$ K ; $T_r = 300$ K ; $m_o = 1.47 \times 10^{-4}$, $\Gamma_o = 10^4$ s^{-1} ; $G_o = 0.315$ e V ; $k_o = 9.23$; $f_1 = 7$; $\tau_o^* = 520$ MPa ; $n=2$; $f_o = 0.05$; $\rho_o = 6.2 \times 10^8$ cm^{-2} ; $q = 4/3$; $p = 3/4$. Those constants are representative for a mild steel XC18 (French Standards) after annealing, 0.17% C ; 0.58% Mn ; 0.21% Si.

Numerical calculations were performed using the same finite difference procedure depicted previously, but the hight of the layer was assumed $h = 2.0$ mm and the number of elementary sublayers was assumed 100, so that the elementary sublayer had the thickness $\Delta h = 20$ μm. With such value of Δh an analysis of the terminal thickness of the ASB could be attempted.

Results of seventeen computer simulations for different nominal strain rates, 80 s$^{-1} \leq \dot{\Gamma}_n \leq 4.5 \times 10^4$ s^{-1}, will be briefly presented here. The nominal instability strain Γ_c and the nominal localization strain Γ_{LOC} are shown as a function of log $\dot{\Gamma}_n$ in Fig. 3. The minimum of the instability strain Γ_c is found again in the region of nominal strain rates above 10^2 s^{-1}, log $\dot{\Gamma}_n = 2.3$, $\dot{\Gamma}_n = 200$ s^{-1}. This is better visible in Fig. 4 with expanded scale of Γ_c. The stabilizing effect of strain rate and perhaps inertia are clearly shown in Fig. 5 where the ratio Γ_c/Γ_{LOC} is plotted as a function of log $\dot{\Gamma}_c$. The ratio begins with value around 2.0 at $\dot{\Gamma}_n = 10^2$ s^{-1} and ends with ~ 6.0 at $\dot{\Gamma}_n = 10^5$ s^{-1}. Around the range of the nominal strain rates ~ 5×10^4 s^{-1} the maximum temperature at the center of the ASB is found to be quite close to the melting point for iron, $T_m = 1785$ K. This is why the last point of localization strain Γ_{LOC} calculated for the highest $\dot{\Gamma}_n$ is on the same level in Fig. 3 as the preceding point, $\Gamma_{LOC} = 2.5$. A high probability that at the latest stages of ASB formation the temperature at the central parts of ASB's exceeds the melting point was suggested in [42]. It was found after examination of fracture surfaces formed during tensile tests of high strength steels that the tops of the dimples separated by a fast shearing are spheroidized, apparently from melting temperature.

The most sensitive parameter for numerical analyses of the ASB's is the final width of the band. In the present analysis a gradient method was assumed to define the final width of shear

band. The profiles of shear strain Γ (y) and temperature T (y) as shown in Fig. 6 and Fig. 7 for $\dot{\Gamma}_n$ = 10^3 s^{-1} and for different levels of the nominal strains Γ_n, served as a basis for all strain rates analysed to find strain and temperature gradients g_Γ (y) and g_T (y) at different levels of the nominal strain. The strain gradients g_Γ (y) obtained after such procedure for $\dot{\Gamma}_n$ = 10^3 s^{-1} at different levels of nominal strain are shown in Fig. 8. The width of the ASB has been defined as an asymptotic value of the distance between the gradient maxima,

$$\lim_{\Gamma \to \Gamma_{LOC}} \Delta y_m = 2a \quad \text{or} \quad \lim_{T \to T_{LOC}} \Delta y_m = 2a \qquad (36)$$

where Δy_m is the distance between the gradient maxima, both for strain and temperature. Fig. 9 shows details how the asymptotic half-value a of the ASB thickness was determined. The dashed line shows terminal evolution of the band thickness. The same procedure was applied to the temperature gradients. The final result is shown in Fig. 10 where the asymptotic values of the shear band width 2a is plotted versus logarithm of the nominal strain rate, log $\dot{\Gamma}_n$. The points depict values of the band width obtained by deformation gradients, stars are obtained by the temperature gradient method. Differences between those two approaches increase when the nominal strain rate decreases. This is due to a more intensive effects of heat conduction at lower strain rates. The shear band widths were found to have a minimum $2a_{min}$ = 140 µm at $\dot{\Gamma}_n$ = 3.2x10^3 s^{-1}. Fig. 10 shows also that at lower strain rates the shear bands are more diffused. At high strain rates inertia and rate sensitivity may again increase the width of ASB's. However, the dimensions of the widths are in general agreement with experimental observations for annealed mild steels, including XC18 one. Some steels with a high yield stress and low strain hardening may narrow substantially the ASB widths. For example, it has been found in [13] that the shear band width is about 20 µm for HY-100 low alloy steel tested at $\dot{\Gamma}_n$ = 1.6x10^3 s^{-1}.

Seventeen computer simulations of deforming layer with thickness h = 2.0 mm and with adiabatic boundary conditions, for seventeen values of the nominal strain rate $\dot{\Gamma}_n$, 80 s^{-1} ≤ $\dot{\Gamma}_n$ ≤ 10^5 s^{-1}, have revealed existence of the strain rate range within which the development of the catastrophic shear is the most easiest. This region is around the nominal strain rate of 10^3 s^{-1}. Also this study has confirmed existence of the minimum of both, the instability strain and the final localization strain, reported earlier in [34] and in [32]. The minimum of the ASB thickness was also revealed at the nominal strain rate $\dot{\Gamma}_n$ = 3.2x10^3 s^{-1}. Evolution of the critical values Γ_c, Γ_{LOC} and 2a at different nominal strain rates found from the numerical simulation has provided a strong argument for experiment in this area.

New experimental technique of impact shearing

The torsion tests of thin-walled tubular specimens are very effective method to study advanced plastic deformation, for both, quasi-static and dynamic loadings. In the literature three

types of torsion devices are reported : the rotary flywheel machines, the high-speed hydraulic testing machines and the SHTB. All those systems of loading have its limitations. For example, SHTB technique has a strong limitations in maximal strain (the net angle of rotation), maximum nominal strain rate of the order $\dot{\Gamma} \approx 2 \times 10^3$ s^{-1} (for a standard specimen length), as well the variation of strain rate during the test are quite high. At high strain rates the finite risetime of the incident wave may cause relatively large specimen deformation during the absence of mechanical equilibrium between incident and transmitter bars.

Another experimental technique, very useful in material testing, is the double shear test introduced by Ferguson et al. (1967) and perfected by Campbell and Ferguson (1970). Since one of the promising specimen geometries to study dynamic plasticity and ASB's is the Double-notch Shear specimen, it has been decided to use this concept in shear testing at medium and high strain rates. Originally, Campbell and Ferguson applied the loading scheme consisted with the incident Hopkinson bar and transmitter Hopkinson tube to study the temperature and strain-rate dependence of the yield stress of a mild steel. Interpretation of oscillograms was the same as for Split Hopkinson Pressure Bar (SHPB or original Kolsky apparatus). Due to combination of a small gage length, $L_s \approx 0.84$ mm, that is the shearing part of the DS specimen, and a standard risetime in the incident bar, $t_r \approx 20$ µs, relatively advanced plastic deformation was reached during the risetime period. This negative feature of the bar/tube configuration was recently discussed in [43].

It was decided, then, to develop a new experimental technique based on a Modified Double Shear specimen. The new experimental technique combines several positive factors already experienced with the other setups. This new technique has been described in some details elsewhere, Klepaczko, [26, 43]. The scheme of the loading setup and measuring devices are shown in Fig. 11. The direct impact was applied to load the MDS specimen. In this way the risetime in specimen loading present in the bar/tube configuration is practically eliminated. The flat-ended projectiles of different lengths made of maraging steel and of diameter $d_p = 10$ mm are launched from an air gun with desired velocities V_o, 1 m/s $\leq V_o \leq$ 200 m/s. The impact velocity is measured by the setup consisting of three sources of light, fiber optic leads 1, 2, 3 and three independent photodiodes. The time intervals of dark signals from the photodiodes generated during passage of a projectile are recorded by two time counters. The setup with three light axes makes it possible to determine acceleration/deceleration of a projectile just before impact, thus, an exact value of V_o can be determined.

Axial displacement U_s (t) of the central part of the MDS specimen is measured as a function of time by an optical extensometer E, acting as an non-contact displacement gage. The optical extensometer reacts to the axial movement of a small black and white target cemented to the central part of the MDS specimen.

Axial force transmitted by the specimen symmetric supports can be determined as a function of time from the transmitted longitudinal wave ε_T (t) measured by strain gages T_1, DC supply unit S_1 and amplifier A_1. All electric signals are recorded by digital oscilloscope DO and next stored in

types of torsion devices are reported : the rotary fly wheel machines, the high speed hydraulic testing machines and the SHTB. All those systems of loading have its limitations. For example, SHTB technique has a strong limitations in maximal strain (the net angle of rotation), maximum nominal strain rate of the order $\dot{\Gamma} = 2 \times 10^3$ s^{-1} (for a standard specimen length), as well the variation of strain rate during the test are quite high. At high strain rates the finite risetime of the incident wave may cause relatively large specimen deformation during the absence of mechanical equilibrium between incident and transmitter bars.

Another experimental technique, very useful in material testing, is the double shear test introduced by Ferguson et al. (1967) and perfected by Campbell and Ferguson (1970). Since one of the promising specimen geometries to study dynamic plasticity and ASB's is the Double-notch Shear specimen, it has been decided to use this concept in shear testing at medium and high strain rates. Originally, Campbell and Ferguson applied the loading scheme consisted with the incident Hopkinson bar and transmitter Hopkinson tube to study the temperature and strain-rate dependence of the yield stress of a mild steel. Interpretation of oscillograms was the same as for Split Hopkinson Pressure Bar (SHPB or original Kolsky apparatus). Due to combination of a small gage length, $L_s = 0.84$ mm, that is the shearing part of the DS specimen, and a standard risetime in the incident bar, $t_r \approx 20$ μs, relatively advanced plastic deformation was reached during the risetime period. This negative feature of the bar/tube configuration was recently discussed in [43].

It was decided, then, to develop a new experimental technique based on a Modified Double Shear specimen. The new experimental technique combines several positive factors already experienced with the other setups. This new technique has been described in some details elsewhere, Klepaczko, [26, 43]. The scheme of the loading setup and measuring devices are shown in Fig. 11. The direct impact was applied to load the MDS specimen. In this way the risetime in specimen loading present in the bar/tube configuration is practically eliminated. The flat-ended projectiles of different lengths made of maraging steel and of diameter $d_p = 10$ mm are launched from an air gun with desired velocities V_o, 1 m/s $\leq V_o \leq$ 200 m/s. The impact velocity is measured by the setup consisting of three sources of light, fiber optic leads 1, 2, 3 and three independent photodiodes. The time intervals of dark signals from the photodiodes generated during passage of a projectile are recorded by two time counters. The setup with three light axes makes it possible to determine acceleration/deceleration of a projectile just before impact, thus, an exact value of V_o can be determined.

Axial displacement U_s (t) of the central part of the MDS specimen is measured as a function of time by an optical extensometer E, acting as an non-contact displacement gage. The optical extensometer reacts to the axial movement of a small black and white target cemented to the central part of the MDS specimen.

Axial force transmitted by the specimen symmetric supports can be determined as a function of time from the transmitted longitudinal wave ε_T (t) measured by strain gages T_1, DC supply unit S_1 and amplifier A_1. All electric signals are recorded by digital oscilloscope DO and next stored in

the computer hard disc. In addition, a hard copy of the recorded signals can be produced with an XY recorder or a printer. This new configuration of experimental setup permits for a wide variation of the nominal strain rate. Direct determination of the axial displacement permits also for a more exact evaluation of deformation history, a very important piece of information in development of adiabatic shear bands. After elimination of time a force-displacement curve can be constructed for the MDS specimen and next $\tau(\Gamma)$ or $\Gamma(\Gamma)$ curves can be determined. The experimental technique described above has appeared quite effective and flexible for material testing at high strain rates as well as for studies of adiabatic shear bands. Detailed description of this technique including calibration of the MDS specimen by FE is given elsewhere, [43].

The net displacement δ_s imposed on the central part of the MDS specimen is

$$\delta_s(t) = \delta_A(t) - C_0 \int_s^t \varepsilon_T(\vartheta) d\vartheta \tag{37}$$

where $\delta_A(t)$ is displacement measured by the optical extensometer/displacement gage shown by E in Fig. 11, $\varepsilon_T(t)$ is the transmitted wave signal, measured by the strain gage T_1 cemented on the transmitter tube surface, C_0 is the elastic wave speed in the tube. If h is the deforming gage length of the MDS specimen, the nominal shear strain can be found from the formula

$$\Gamma(t) = \frac{1}{h}\left[\delta_A(t) - C_0 \int_s^t \varepsilon_T(\vartheta) d\vartheta \right] \tag{38}$$

The nominal strain rate can be found also

$$\dot{\Gamma}(t) = \frac{1}{h}\left[\frac{d\delta_A}{dt} - C_0 \varepsilon_T(t) \right] \tag{39}$$

It is assumed in the elementary approach that the transmitted signal $\varepsilon_T(t)$ in the Hopkinson tube is sufficient to find the axial force transmitted by the MDS supports into the tube

$$F(t) = E A_E \varepsilon_T(t) \tag{40}$$

where A_E is the cross section of the tube and E is Young's modulus. The cross section A_E is related to the external and internal tube diameter

$$A_E = \frac{\pi}{4}(D^2 - d^2)$$

The shear stress in the MDS specimen can be found from the formula, [43]

$$\tau(t) = \xi \frac{F(t)}{2ab} \tag{41}$$

where a b is the active cross section of one side of the MDS specimen, ξ is the calibration factor, $\xi \geq 1$, and F is the axial force in the Hopkinson tube. The final formula for the shear stress is

$$\tau(t) = \frac{\pi(D^2 - d^2)\xi E}{8\,a\,b}\,\varepsilon_T(t)$$

(42)

Thus, the shear stress in the MDS specimen is proportional to the current signal of the transmitted longitudinal wave ε_T. All those relations have been derived using the elementary wave theory of longitudinal elastic waves. In addition, it was assumed in derivation of eq. (15) that the local pressures applied by MDS specimen at the end of the Hopkinson tube are transmitted uniformly at the distance $x \approx 3D$, this is dynamic St. Venant rule. At the impact velocity $V \approx 100$ m/s time to fracture of the MDS specimen is relatively short, for example, for $\Gamma_{cr} = 1.0$ the time to fracture is $t_{cr} \approx 20$ μs, it gives the wavelength $\lambda \approx 100$ mm and the relative wavelength $\bar{\lambda} = 2\lambda/(D-d)$; is $\bar{\lambda} = 11.1$; $D = 32$ mm and $d = 14$ mm. Those wavelengths indicate that some geometric dispersion may be present, but the so-called Pochhammer-Chree vibrations, and of course geometric dispersion, are much smaller in a tube of the same external diameter than in a solid bar, [44]. A more exact analyses of wave dispersion in tubes are in progress and some of them are discussed in the next part of this report.

Another important parameter is the length of projectile L_p. It is desirable to reach the time to fracture t_r during the first cycle of elastic wave propagation in a projectile. If the nominal strain rate Γ is assumed and the critical shear strain Γ_{cr} can be estimated, the length of the projectile L_p which assures the contact with the MDS specimen up to fracture can be found from the formula

$$L_p = \frac{\Gamma_{cr}}{2\Gamma}\,C_o$$

(43)

For example, when $\Gamma_{cr} = 1.0$ and $\Gamma = 5 \times 10^4$ s^{-1} the projectile length is reduced to $L_p = 50$ mm, but for $\Gamma = 10^3$ s^{-1} the length should be $L_p = 2500$ mm. It appears that at lower strain rates it is almost impossible to deform and fracture the MDS specimen during the contact time $t_p = 2L_p/C_o$. The longest projectile used in this study was $L_p = 400$ mm. For example, in Fig. 12 and Fig. 13 are respectively shown original oscillogrammes for a mild (XC18) and a hard steel (VAR4340). The period of time to fracture the mild steel specimen at impact velocity $V_o = 35$ m/s was ~ 260 μs, whereas a more brittle specimen is broken at the impact velocity ~ 160 m/s within ~ 20 μm.

Nevertheless, the elementary wave theory can be applied, as the first approach, to obtain a complete information on the whole process of deformation and fracture of the MDS specimen, the following data can be obtained from one test : $\tau(t)$; $\Gamma(t)$; $\Gamma(t)$; $\tau(\Gamma)$ and $\Gamma(\Gamma)$. Since a two-channel fast digital oscilloscope was used (sampling rate 1GHz), the useful portion of the digital memory could be taken for analysis to determine all needed functions. A computer program was prepared to calculate all those functions.

Propagation of elastic longitudinal waves in tubes, the Hopkinson tube, analytic solutions

It was shown in the previous Chapter that for the case of a hard MDS specimen and at relatively high impact velocity the total time to fracture may be as short as ~ 20 μs. When fracture occurs in such a short time it may expected that some dispersive effects can be present during transmission of the elastic signals between MDS specimen and the strain gage SR, Fig. 11. This distance in the configuration used was $\Delta x_g \cong 170$ mm, i.e. about five external diameters of the Hopkinson tube.

It is then of interest to study the elastic wave dispersion in tubes. The problem has been divided into two separate studies. The first one concentrated on analytic solutions for two specific boundary value problems, that is for the mixed problem of imposed pressure on a semi-infinite circular tube and the next one is devoted to the longitudinal impact (initial conditions in velocity).

The problem of imposed pressure at the end of semi-infinite circular tube has been solved analytically by use of the double integral transforms (Fourier and Laplace transform). This method leads to solutions given in the terms of Fourier and Laplace integrals.

A similar mixed-pressure problems of semi-infinite circular rods were solved previously in [45].

The second problem solved is the impact on a semi-infinite circular elastic tube where the axial velocity is imposed instantaneously at the end of the tube. The solution is obtained under assumption that the end of the tube has no tangential stresses but is suddenly set into motion with a constant velocity and the lateral surfaces are free of stresses. The analogous problem for a semi-infinite bar was solved in [46]. The method applied in [46] was to split the problem into two parts. In the first part the collision of two half-spaces was considered. In the second part an infinite bar was considered with an equal and opposite stresses travelling along the lateral surface. Using the principle of superposition a stress free lateral surface was ensured. The method presented in [46] has been adopted to the problem of a semi-infinite circular tube loaded by impact.

Both solutions for a tube, which are mentioned above, are reported in details in the Appendix N° 2 to this Report, [47].

Here only a brief description of those solutions will be given.

A semi-infinite cylindrical elastic tube of inner radius a and outer radius b, which are referred to the cylindrical coordinates (r, θ, z), where the z-axis coincides with the of the tube, is considered. Let λ, μ be Lame constants and ρ be the mass density of the tube material. The motion is restricted to the axisymmetric case, thus the displacement vector $\underline{U}$ is independent of the circumferential variable θ and

$$\underline{U}\ (r,z,t) = (U_r\ (r,z,t))\ ;\ 0\ ;\ U_2\ (r,z,t) \tag{44}$$

The equations of motion of the linear elasticity in the cylindrical coordinates take the form

$$\left(\lambda + 2\mu\right)\left(\frac{\partial^2 u_r}{\partial r^2} + \frac{1}{r}\frac{\partial u_r}{\partial r} - \frac{u_r}{r^2} + \frac{\partial^2 u_z}{\partial r\,\partial z}\right) + \mu\left(\frac{\partial^2 u_r}{\partial z^2} - \frac{\partial^2 u_z}{\partial r\,\partial z}\right) = \rho\,\frac{\partial^2 u_r}{\partial t^2}\,,$$

$$\left(\lambda + 2\mu\right)\left(\frac{\partial^2 u_r}{\partial r\,\partial z} + \frac{1}{r}\frac{\partial u_r}{\partial z} + \frac{\partial^2 u_z}{\partial z^2}\right) - \mu\,\frac{1}{r}\left(\frac{\partial u_r}{\partial z} - \frac{\partial u_z}{\partial r}\right) -$$

$$\mu\left(\frac{\partial^2 u_r}{\partial z\,\partial r} - \frac{\partial^2 u_z}{\partial r^2}\right) = \rho\,\frac{\partial^2 u_z}{\partial t^2}\,.$$

(45)

Consider the boundary conditions

$$\sigma_{zz}\,(r,z=0,t) = -\,f\,(t)\,.$$

(46)

$$u_r\,(r,z=0,t) = 0\,,\ \text{for}\ r \in \langle a,b\rangle\,,\ t \in (0,\infty)$$

and

$$\sigma_{rr}\,(r=a,z,t) = \sigma_{rr}\,(r=b,z,t) = 0\,.$$

(47)

$$\sigma_{rz}\,(r=a,z,t) = \sigma_{rz}\,(r=b,z,t) = 0\,,\ \text{for}\ z \in (0,\infty)\,,\ t \in (0,\infty)\,.$$

where $f\,(.)$ is a given function, provided that $f\,(t) = 0$ for $t < 0$. A further condition is that the displacements and the stresses vanish at infinity, $z \to \infty$. Assuming that the semi-infinite circular tube is at rest prior to time instant $t = 0$, equations (46) and (47) are supplemented by the initial conditions

$$u_r\,(r,z,t=0) = \frac{\partial u_r}{\partial t}\,(r,z,t=0) = 0\,.$$

(48)

$$u_z\,(r,z,t=0) = \frac{\partial u_z}{\partial t}\,(r,z,t=0) = 0\,,\ \text{for}\ r \in \langle a,b\rangle\,,\ z \in (0,\infty)\,.$$

The set of equations (45) along with the initial and boundary conditions (46) and (47) has been solved by introduction of the displacement potentials, details are given in [48]. The solution by integral transforms has been found using the inversion theorems of the Laplace and Fourier transforms, the solution can be written in the form

$$u_r(r,z,t) = \frac{1}{\pi^2 i} \int_0^\infty \int_{-\infty}^\infty \bar{u}_r^s(r,\xi,p)\, e^{pt} \sin(\xi z)\, dp\, d\xi,$$

$$u_z(r,z,t) = \frac{1}{\pi^2 i} \int_0^\infty \int_{-\infty}^\infty \bar{u}_z^c(r,\xi,p)\, e^{pt} \cos(\xi z)\, dp\, d\xi,$$

$$\sigma_{rr}(r,z,t) = \frac{1}{\pi^2 i} \int_0^\infty \int_{-\infty}^\infty \bar{\sigma}_{rr}^s(r,\xi,p)\, e^{pt} \cos(\xi z)\, dp\, d\xi,$$

$$\sigma_{rz}(r,z,t) = \frac{1}{\pi^2 i} \int_0^\infty \int_{-\infty}^\infty \bar{\sigma}_{rz}^s(r,\xi,p)\, e^{pt} \sin(\xi z)\, dp\, d\xi,$$

$$\sigma_{zz}(r,z,t) = \frac{1}{\pi^2 i} \int_0^\infty \int_{-\infty}^\infty \bar{\sigma}_{zz}^s(r,\xi,p)\, e^{pt} \sin(\xi z)\, dp\, d\xi.$$

(49)

The function $f(.)$, if the boundary condition is given as (46), is yet undefined. The possibility of the following cases of impulses can be mentioned :

a. infinitely short impulse, $f(t) = - f_0\, \delta(t)$, where f_0, $f_0 > 0$, is a constant and $\delta(.)$ is the Dirac function ;

b. infinitely long impulse, $f(t) = - f_0\, H(t)$, where $H(.)$ is the Heaviside step function ;

c. impulse of finite length, $f(t) = - f_0\, H(\tau - t)$, where τ, $\tau > 0$, is the duration of the impulse.

The second boundary value problem studied was the longitudinal impact which was reduced to the mixed conditions of shock pressure at the end of the semi-infinite circular elastic tube. Two semi-infinite circular tubes, moving in opposite directions with velocity v, are assumed to contact at the instant $t = 0$ and at the plane $z = 0$. The lateral surfaces of tubes are free of stresses.

The solution of the problem considered is devided by application of the superposition principle for two separate problems. The first of them is limited to two elastic semi-spaces, moving in opposite directions with velocity v. They are assumed to contact at the instant $t = 0$ and at the plane $z = 0$. After time $t = 0$ the semi-spaces are assumed to behave as a single, solid space which are assumed to behave for $t > 0$ as a single, infinite tube. The solution of this problem is given in [46]. The initial conditions are:

$u_r (r,z,t) = 0$,

$$u_z (r,z,t) = \begin{cases} \pm v\, t & \text{for } \pm z > c\, t_1 \\ - v\, z/c_1 & \text{for } |z| < c_1 t \end{cases} \qquad (50)$$

The displacements assumed above induce the following stresses, [47]

$\sigma_{zr} (r,z,t) = 0$,

$$\sigma_{zz} (r,z,t) = \begin{cases} 0 & \text{for } |z| > c_1 t \\ - (\lambda+2\mu)\, v/c_1 & \text{for } |z| < c_1 t \end{cases}$$

$$\sigma_{rr} (r,z,t) = \begin{cases} 0 & \text{for } |z| > c_1 t \\ - \lambda\, v/c_1 & \text{for } |z| < c_1 t \end{cases} \qquad (51)$$

It is seen from equations (51) that the solution of the first problem causes non-zero radial tractions on the lateral surfaces of the circular tube. Applying the principle of superposition to ensure a stress free lateral surfaces of the infinite tube the second problem is considered, which is defined by equations of motion (45), the boundary conditions

$$\sigma_{zr} (r=a,z,t) = \sigma_{zr} (r=b,z,t) = 0 ,$$

$$\sigma_{rr} (r=a,z,t) = \sigma_{rr} (r=b,z,t) = \begin{cases} 0 & \text{for } |z| > c_1 t \\ - \lambda\, v/c_1 & \text{for } |z| < c_1 t \end{cases} \qquad (52)$$

$$\text{for } z \in (-\infty, +\infty) , \; t \in (0, +\infty) ,$$

and the initial conditions given in (50) for $z \in (-\infty, +\infty)$. A further condition is that the displacements and the stresses vanish when $|z| \to \infty$.

The solution of the problem is found by using displacement potentialy and Fourier exponential transforms, as well as Laplace transform. Using the inversion theorems of the Laplace and Fourier exponential transforms the solution can be written in the form

$$u_r(r,z,t) = \frac{1}{4\pi^2 i} \int \int_{-i\infty}^{\gamma+i\infty} \overline{u}_r^F(r,\xi,p)\, e^{i\xi z} e^{pt}\, dp\, d\xi,$$

$$u_z(r,z,t) = \frac{1}{4\pi^2 i} \int \int_{-i\infty}^{\gamma+i\infty} \overline{u}_z^F(r,\xi,p)\, e^{i\xi z} e^{pt}\, dp\, d\xi,$$

$$\sigma_{zz}(r,z,t) = \frac{1}{4\pi^2 i} \int \int_{-i\infty}^{\gamma+i\infty} \overline{\sigma}_{zz}^F(r,\xi,p)\, e^{i\xi z} e^{pt}\, dp\, d\xi,$$

(53)

$$\sigma_{zr}(r,z,t) = \frac{1}{4\pi^2 i} \int \int_{-i\infty}^{\gamma+i\infty} \overline{\sigma}_{zr}^F(r,\xi,p)\, e^{i\xi z} e^{pt}\, dp\, d\xi,$$

$$\sigma_{zz}(r,z,t) = \frac{1}{4\pi^2 i} \int \int_{-i\infty}^{\gamma+i\infty} \overline{\sigma}_{zz}^F(r,\xi,p)\, e^{i\xi z} e^{pt}\, dp\, d\xi.$$

The solutions (44) and (53) enable to calculate effects of dispersion for idealised impulses, type Dirac and square of infinite and finite lengths.

Propagation of elastic longitudinal waves in tubes, the Hopkinson tube, numerical study

Although analytic solutions have been found for an elastic semi-infinite tube loaded instantaneously by pressure or by velocity, the real case with MDS specimen attached to the front of the Hopkinson tube is still more complicated, mostly due to non-symmetric circumferential distribution of pressures. Such a case is impossible to solve analytically, and hence, series of numerical studies have been undertaken using a dynamic FE code. A non-symmetric distribution of pressures have been assumed at the face of the tube in the form of two contact areas of the MDS specimen, that is $a = R - r$, $a = 9.0$ mm, where R is the outer radius and r is the inner radius, $b = 6.0$ mm, where b is the thickness of the MDS specimen. The total area by which the total force is transmitted is $A \approx 2ab$. This is shown in Fig. 14. In Fig. 15 are shown all cases of trapezoidal pulses assumed at the end of the tube on the shadowed surfaces 2ab.

The following material constants were assumed for the Hopkinson tube, $E = 2.1 * 10^5$ MPa, $v = 0.3$ and $\rho = 7.85$ g/cm^3. The Hopkinson tube has been modelled as semi-infinite by its artificial extension with a very low wave speed and the same impedance. Thus, all reflections from the other side of the tube have been eliminated. Comparison of calculations with a normally extended tube by FE (the same C_o, and ρ) revealed only small differences between those two cases.

Since the main interest is concentrated on high impact velocities imposed on MDS specimens, $V_o \approx 100$ m/s, the cases $N° 1$ and $N° 4$ will be briefly discussed in this Report. Case $N° 1$ is assumed as $p_{max} = 450$ MPa, $t_r = 20$ μs ; $t_o = 10$ μs and $t_a = 20$ μs. The results of FE calculations in the form of longitudinal strain $\varepsilon_1(t)_x$ and $\varepsilon_2(t)_x$, where ε_1 is the longitudinal strain at the outer surface of the Hopkinson tube, and ε_2 at the inner surface, are shown in Fig. 16a/16b for $x_1 = 90.5$ mm ($\sim$ 3D of the tube) and in Fig. 17a/17b for $x_2 = 170.5$ mm ($\sim$ 5D). In each figure a and b the results are shown for the external surface of the tube (solid line) and the internal surface (broken line). In addition, figures a are obtained for the vertical plane from Fig. 14a, that is the plane in which the MDS specimen is attached. Whereas figures b refer to the time-distribution of longitudinal strains ε_1 and ε_2 at the same distances x_1 and x_2 but with 90° orientation.

Those figures indicate the existence of higher modes of vibrations excited by a non-symmetric impact. This is visible for both distances studied. The FE calculations reveal also small differences between time-distributions of longitudinal strain obtained on external and internal surface of the Hopkinson tube. The origin of those differences are unknown, and they may be caused by the FE technique itself. Further studies are needed at this point, perhaps with different meshing. The assumed risetime of the incident pulse was $t_r = 20$ μs, this risetime is slightly distorted at the beginning for both distances $x_1 = 90.5$ mm and $x_2 = 170$ mm by a small inflection. The descending part of the incident pulse, assumed originally as $t_a = 20$ μs, is slightly delayed. The results obtained for the distance $x_2 = 170.5$ mm do not differ much from the previous ones for x_1. The transmitted wave determined from the tube surface is equally dispersed, and the differences in waves between external and internal surfaces are small. Again, this needs further studies for less idealized impulses.

The most important conclusion drawn from the FE calculation of the case $N° 1$ is that the level of the mean stress of the plateau determined from the surface of the Hopkinson tube agrees with the assumed level of pressure p_{max} multiplied by the ratio of surfaces,

$$\sigma_m = \frac{\pi (D^2 - d^2)}{8 a b} p_{max} \; ; \; \sigma_m = \xi \, p_{max} \tag{54}$$

The ratio ξ in the real case of Hopkinson tube is $\xi \sim 0.2$. This fact permits for determination of the critical stress imposed on the MDS specimen via the peak of strain measured by the Hopkinson tube, in the real case the strain gages are cemented at $x \sim 170$ mm.

The most interesting case is the $N° 4$, because during testing of hard steels the order of t_r, t_o and t_a are similar as assumed for the $N° 4$: $t_r = 5$ μs, $t_o = 5$ μs and $t_a = 5$ μs, however, $p_{max} \sim 450$

MPa is rather a small value in comparison to the real ones for a hard steels with the flow stress $\sigma =$ 1000 MPa. The results of those FE calculations are shown in Fig. 18 and Fig. 19. The same approach was used as for the case N° 1. Again, the analysis of amplitudes indicates that even for such short pulses the maximum stresses determined in MDS specimen after the back extrapolation are correct. At the distance x_1 = 90.5 mm the rising part of the pulse shows at the beginning a small inflection, overall this figure resembles the oscillogram for VAR4340 steel shown in Fig. 13. At the distance x_2 = 170.5 mm the pulse is slightly wider due to geometry dispersion, but the mean value of strain also permits for back extrapolation to find MDS stresses. The tails of the pulses for both distances show large amplitude vibrations which resemble to some extend measurements (Fig. 13). Since the assumed values of p_{max} were relatively low in comparison to the real levels of stresses in tested 4340 steel, another series FE calculations have been run for Cases N° 1 and N° 4, but with p_{max} = 1000 MPa and the same values of t_r, t_o and t_a. Those calculations have confirmed validity of the procedure of back extrapolation of stresses for MDS specimens. The relative level of vibrations is reduced in comparison to the main pulse. This is also observed for the tails of the calculated waves. Other calculations gave very similar results.

The main conclusion drawn from FE dynamic calculations is the confirmation of the back extrapolation procedure to find stresses imposed on MDS specimens by direct impact using eq. (54).

Numerical analysis of Modified Double-Shear specimen and specimen calibration

The new configuration of experiment with the MDS specimen, as it is shown in Fig. 12 has been developed in LPMM-Metz. The modified specimen geometries are shown in Fig. 20a and 20b. The modified geometries have a wider gage length, l_s = 2.0 mm. in comparison to [48], which substantially reduce stress concentrations near the notch corners.

The external part are longer and those parts are clamped to the transmitter tube to prevent rotations. The MDS geometry was analysed by FE technique at different stages of plastic deformation. The total number of elements for half of the MDS specimen was 640. Around and within deforming part of the specimen the mesh was much denser, 460 elements. The central part of the MDS specimen was assument to deplace uniformly. Since the width of the plastically deformed parts of the MDS specimen is only 6.0 mm and the shear stress τ_s is supposed to be determined for an infinite layer, a calibration factor ξ must be introduced, thus

$$\tau = \xi \tau_s \qquad \xi \geq 1 \qquad\qquad (55)$$

where τ_s is the mean stress in the deformed section of the MDS specimen. Distribution of the shear stresses at the nominal shear strain Γ_s = 2.5 x 10^{-3} is shown in Fig. 21a whereas Fig. 21b shows distribution for Γ_s = 0.5. Distributions of the shear strains for the same values of Γ_s are shown in

Fig. 22a and 22b. All FE calculations have been performed for the quasi-static stress-strain relation, which depicts more or less exactly tensile behavior of low alloy steel XC18 at strain rate $\varepsilon \approx 10^{-3}$ s^{-1}

$$\sigma = \sigma_y + B\left[\left(\varepsilon - \frac{\varepsilon_y}{E} + DB^p\right)^n - D^n B^{np}\right], \quad \varepsilon \geq \varepsilon_y \tag{56}$$

with the yield stress and strain : $\sigma_y = 240$ MPa, $\varepsilon_y = 1.165 \times 10^{-3}$;

$$D = \left(\frac{n}{E}\right)^{\frac{1}{1-n}} \qquad ; \qquad p = \frac{1}{1-n}$$

$n = 0.3$; $E = 2.06 \times 10^5$ MPa ; $B = 451.1$ MPa. This is very useful form of $\sigma(\varepsilon)$ relation since it has a smooth transition from the elastic to plastic regions, that is the first derivative $\theta = d\sigma/d\varepsilon$ has no jumps. Of course, in the elastic region $\sigma = E\varepsilon$ for $\varepsilon \leq \varepsilon_y$. The mean value of the stress calibration factor ξ obtained after FE analysis for MDS specimen shown in Fig. 20a is $\xi \approx 1.2$. It was found that ξ slightly increases from $\xi \approx 1.12$ at $\Gamma_s = 0.05$ to $\xi \approx 1.2$ at $\Gamma_s = 0.50$, so the mean value for $0.05 \leq \Gamma_s \leq 1.0$ is ~ 1.2. The distributions of shear strain shown in Fig. 22a and 22b demonstrate that the strain field is quite uniform with a small asymmetry due to bending component from the supports. It was also found, in the real tests as well as from the FE analysis, that the exterior parts of the specimen which are supported also deform plastically, causing an increasing tendency for rotation (MDS specimen, Fig. 20a). This is why the specimen geometry has been slightly modified as it is shown in Fig. 20b. The width of the supports is enlarged to 10 mm and the notch is slightly diper. It is clear that due to modifications introduced into the specimen geometry the axial force versus axial displacement provides a reliable input data to find quasi-static or dynamic $\tau(\Gamma)$ response.

Preliminary experiments. mild steel

It has been decided to perform preliminary series of tests on the mild steel in the recrystallised state. This steel has been assumed as a model material for the numerical calculations and all mechanical tests. In order to perform quasi-static tests and also tests with higher strain rates, of the order 10^3 s^{-1}, a special loading rig has been constructed. The rig, shown in Fig. 23, having its own measuring systems (force is measured by an SR-gages and signal conditioner, and displacement by two LVDT-s and amplifiers), can be fitted to any standard testing machine. The signals $F(t)$ and $\delta_1(t)$, $\delta_2(t)$ could be stored in a digital memory, where F is the axial force, δ_1 and δ_2 are LVDT displacements. Shear stress and shear strain can be obtained from the formulas

$$\tau_s(t) = \frac{F(t)}{2ab} \quad \text{and} \quad \tau(t) = \xi \frac{F(t)}{2ab}$$

(57)

where a and b are respectively the width of the deformed part and specimen thickness, the mean axial displacement is

$$\bar{\delta}_s(t) = \frac{\delta_1(t) + \delta_2(t)}{2} \quad \text{and} \quad \Gamma(t) = \frac{\bar{\delta}_s(t)}{l_s}$$

(58)

where $\bar{\delta}_s$ is the mean axial displacement. Elimination of time from $\tau(t)$ and $\Gamma(t)$ permits for determination of $\tau(\Gamma)\dot{r}$. In addition, the strain rate must be determined from the formula

$$\dot{\Gamma}(t) = \frac{1}{l_s} \frac{d\bar{\delta}_s(t)}{dt}$$

(59)

Application of the closed-loop dynamic testing machine makes it possible to reach for the MDS specimen the strain rate of the order $\dot{\Gamma} = 10^3$ s^{-1}. Of course, the maximum strain rate is a linear function of the axial velocity and proportional to $1/l_s$. Fig. 24 shows log $\dot{\Gamma}$ as a function of gage length l_s for two axial velocities : 20 m/s and 100 m/s. By the broken vertical lines are marked the gage lengths $l_s = 0.25$ mm and 0.84 mm, used in [48, 49], and $l_s = 2.0$ mm used in the MDS specimen. For example, in the case of impact velocity 100 m/s and MDS specimen the nominal strain rate $\dot{\Gamma}$ is 5×10^4 s^{-1} is reached. Thus, the new experimental technique can cover also the high strain rate region, 10^3 s^{-1} $\leq \dot{\Gamma} \leq 10^5$ s^{-1} (2.0 m/s $\leq V \leq 200$ m/s).

First series of experiments were performed on low-alloy steel XC18 (French Standards) of the following composition in % : C 0.17 : Mn 0.58 ; Si 0.21 ; S 0.032 ; P 0.024. The specimen material was supplied in the form of cold drawn bars DIA 12 mm. After precision machining, all specimens were vacuum annealed at ~ 1000 K for 1½ hrs and furnace cooled. Metallographic examination showed a uniform microstructure with evenly distributed grains of ferrite. The tests on MDS specimens were performed within two ranges of strain rates : medium rates 10^2 s^{-1} $\leq \dot{\Gamma} \leq 10^3$ s^{-1} with closed-loop fast testing machine and high rates 10^4 s^{-1} $\leq \dot{\Gamma} \leq 10^5$ s^{-1} with the new experimental technique. One of oscillograms obtained with impact velocity V = ~ 37 m/s is shown in Fig. 12a. The upper trace comes from the strain gages on the transmitter tube and the lower one from the optical extensometer. It can be seen from Fig. 12a that after the upper yield peak there is a small oscillation on the upper trace, they are believed to be partly caused by the out-of-phase longitudinal vibrations of the transmitter tube revealed by the FE dynamic calculations. Since the length of the projectile was $L_p = 180$ mm with the time of contact $t_p = 74$ μs, around three full cycles of wave reflexions had occured during specimen deformation. They are recognizable in the oscillogram. As a whole, both the upper and lower yield stresses can be found, as well as the plastic flow curve up the fracture by adiabatic shearing. The signal from the optical extensometer

shows that the displacement rate of the central part of the MDS specimen is almost constant. The optical contact was lost before the specimen fractured.

A number of MDS specimens was tested at different impact velocities from 30 m/s to about 100 m/s. The upper yield stress in shear τ_y is plotted in Fig. 25 against the logarithm of shear strain rate $\dot{\Gamma}$. In the region of low strain rates, values of shear stress τ_y were obtained from tensile tests, [39], and transformed into shear by $\tau_y = \sigma_y/\sqrt{3}$ and $\Gamma = \sqrt{3}\ \varepsilon$. In this region the rate sensitivity β is characterized by a small nearly constant slope ; $\beta = \partial\tau_y/\partial\log\dot{\Gamma}$, [31, 48, 50]. In the region of high strain rates a substantial increase of the upper yield stress is observed. This is shown in the linear scale of $\dot{\Gamma}$ in Fig. 26. This feature will be discussed in the further part of this Report. In Fig. 27 the mean values of the lower yield stress τ_{yl} (vibrations are eliminated), obtained for XC18 steel are compared with results for a mild steel reported by Campbell and Ferguson [48] ; composition of En3B (British Standards) steel as given in [48] is : C 0.12 ; Mn 0.62 ; Si 0.10 ; S 0.029. Because of the higher carbon content in XC18 steel the level of the lower yield stresses is overall higher than for En3B steel. On the other hand DS specimen used in [48] with slots 0.84 mm and length of deformed part, a = 3.2 mm, should have a much higher stress calibration factor ξ in comparison to the MDS specimen where $\xi \approx 1.2$. It is also probable that the instantaneous strain rates in DS specimen tested in the SHB (bar and tube) were much lower than the nominal values used in plotting of Fig. 27. This could be a reason why tests with the new technique give higher values of τ_{yl}.

Another comparison was made between results obtained for a high purity iron (99.99% Fe) in [51], where pressure-shear impact experiments were used. Flat specimens with thickness between 300 μm and 3 μm were sandwiched between two hard, parallel plates that are inclined relative to their direction of approach. Nominal stresses and strains in the specimens were determined from elastic wave profiles monitord at the rear surface of one of the hard plates. It is seen in Fig. 28, where the comparison is shown, that at high shearing rates the shear stresses are of the same order, however, similar values for τ_{yl} obtained from MDS specimen occur at strain rate $\dot{\Gamma} \approx 10^5$ s^{-1} and those obtained from pressure shear experiment at $\dot{\Gamma} \approx 10^6$ s^{-1}. General trends in changes of the lower yield stress are similar for both, so different, experimental methods.

It is well known that in the region of low and medium strain rates, 10^{-4} s$^{-1} \le \dot{\Gamma} \le 10^2$ s^{-1}, the rate and temperature sensitivities of flow stress are controlled by the thermally activated kinetics of dislocations, [38, 48, 50]. In this region the rate sensitivity $\beta = (\partial\tau/\partial\log\Gamma)_T$ does not depend on strain rate $\dot{\Gamma}$. However, as it is seen from Fig. 25 and Fig. 27, the high strain rate region, typically 10^3 s$^{-1} \le \dot{\Gamma} \le 10^6$ s^{-1}, is characterized by a rapid increase of β with increasing strain rate. It is commonly assumed, and it was verified in many theoretical and experimental studies, that in BCC structures the instantaneous rate sensitivity β is the result of dislocation movement by the mechanism of the thermally activated formation of kink pairs over Peierls potential, for example, [38, 40, 41, 52]. Since this approach is well known, detailed discussion of its applications will be here omitted.

When, within the region of high strain rates, the yield stress or flow stress are plotted in a linear scale of strain rate, the experimental data can be represented by a stright line, [48]. Experimental points for XC18 steel from Fig. 25 have been transformed in the linear scale of Γ and the final result is shown in Fig. 29 for the case of the upper yield stress and in Fig. 30 for the lower yield stress. Indeed, in both cases the linear approximation fits experimental points. The following linear relation was analysed by the least squares method

$$\tau_y = \hat{\tau}_y + \eta\, \dot{\Gamma}$$

(60)

where $\hat{\tau}_y$ is the threshold stress and η is the pseudo-viscosity. Both yield stresses were analysed and the best linear fit is shown in Figs. 29 and 30 by the broken lines. The complete results of those analyses are given in Table 2, whereas the reanalysed results from ref. [48] are given in Table 3.

Table 2

Steel XC18	$\hat{\tau}_y$ [MPa]	η [kPa.s]	r^2
Upper y. stress	648.1	14.3	0.954
Lower y. stress	508.2	4.0	0.870

Table 3

Steel En 3 B	$\hat{\tau}_y$ [MPa]	η [kPa.s]	r^2
Lower y. stress	241.4	2.1	0.960
$\Gamma = 0.075$	241.7	2.5	0.911
$\Gamma = 0.21$	246.2	2.5	0.924
$\Gamma = 0.38$	249.2	2.6	0.977

Comparison of Tables 2 and 3 shows that values of η for the lower yield stress are of the same order, although MDS specimen loaded by direct impact show η-values almost twice higher. Because of the direct impact loading, with the rise time $1\ \mu s \leq t_i \leq 2\ \mu s$, behavior of the upper yield stress is different for MDS specimens. It is associated with the delay time of plasticity in mild steels. [50].

An early interpretation of the linear relation $\tau\ (\Gamma)_{\Gamma,T}$ is that the stress intercepts at $\Gamma = \Gamma_0$; that is $\hat{\tau}\ (\Gamma)_T$, can be determined by the temperature-dependent threshold stress. When the applied stress τ exceeds the threshold stress, $\tau \geq \hat{\tau}$, the dislocation velocity is controlled by dissipation of energy when dislocation moves through the lattice. It is commonly assumed that this dissipation is

of linear viscous nature, and then the stress component τ_η would be proportional to the mean dislocation velocity $\overline{v}$. Then the viscous drag relation may be expressed in the form

$$\tau_\eta = B \frac{\overline{v}}{b}$$

(61)

where B is a damping constant. When the Orowan relation is introduced into eq. (61), the component τ_η can be expressed in terms of the mean mobile dislocation density ρ_m, and $\dot{\Gamma} = \rho_m b \overline{v}$,

$$\tau_\eta = B \frac{\dot{\Gamma}}{b^2 \rho_m} \quad \text{or} \quad \tau_\eta = \eta \dot{\Gamma}$$

(62)

where $\eta = B/b^2 \rho_m$ is the coefficient of viscosity.

This interpretation has many weak points. The first one is that the thermally activated processes are still operative at high strain rates. A more exact analysis of experimental data obtained by Campbel and Ferguson, [48], were published in [53]. It was concluded in this latter analysis that the whole region of strain rates covered in [48] can be approximated by an unique constitutive relation based on the thermally activated micromechanism of double kink kinetics. This analysis indicates on the possibility that the theory of thermally activated flow is exact enough to describe rate sensitivity of iron and mild steels up to strain rates of the order 10^5 to 10^6 s^{-1}, [53].

Another possibility, and more recent, to explain the pseudo-viscosity lies in the fact that some experimental data clearly indicate that the mechanical threshold $\hat{\tau}_o$ is itself rate sensitive, [54, 55]. Theoretical analyses of structural evolution which can lead to a rate sensitive mechanical threshold were also published recently, [56, 57].

An important observation, directly related to ASB in XC18 steel, are values of the critical total strain (elastic plus plastic) determined as a function of imposed velocity on MDS specimens. The final result is shown in Fig. 31 where the critical shear strains, $\Gamma_m = \delta_m/l_s$, are shown as a function of $\log \dot{\Gamma}$. The mean values are shown as circles. The results for two lowest strain rates, $\dot{\Gamma} \approx 75$ s^{-1} and $\dot{\Gamma} \approx 750$ s^{-1}, were obtained with the loading rig and the fast closed-loop machine, the data for three highest strain rates in the range 1.8×10^4 s$^{-1} \leq \dot{\Gamma} \leq 4.7 \times 10^4$ s^{-1}, were obtained with the new experimental technique. The impact velocity at the highest nominal strain rate was ~ 100 m/s.

Since the dimensions of deforming parts of the MDS specimen are the same as the thickness of the layer studied by numerical methods, and the same steel was assumed for the numerical study, a direct comparison is possible between experimental results shown in Fig. 31 and numerical results of Fig. 3. Although values of localization strains are overall smaller than the critical strains found by experiment, at lower strain rates the same trend is observed, that is the total shear strain increases as a function of $\log \dot{\Gamma}$. However, it is clear that at the highest strain rates an abrupt drop in the critical strain occurs. For example, the mean value of the critical strain from six tests

of linear viscous nature, and then the stress component τ_η would be proportional to the mean dislocation velocity $\overline{v}$. Then the viscous drag relation may be expressed in the form

$$\tau_\eta = B \frac{\overline{v}}{b} \tag{61}$$

where B is a damping constant. When the Orowan relation is introduced into eq. (61), the component τ_η can be expressed in terms of the mean mobile dislocation density ρ_m, and $\dot{\Gamma} = \rho_m \, b \, \overline{v}$,

$$\tau_\eta = B \frac{\dot{\Gamma}}{b^2 \rho_m} \quad \text{or} \quad \tau_\eta = \eta \, \dot{\Gamma} \tag{62}$$

where $\eta = B/b^2 \rho_m$ is the coefficient of viscosity.

This interpretation has many weak points. The first one is that the thermally activated processes are still operative at high strain rates. A more exact analysis of experimental data obtained by Campbel and Ferguson, [48], were published in [53]. It was concluded in this latter analysis that the whole region of strain rates covered in [48] can be approximated by an unique constitutive relation based on the thermally activated micromechanism of double kink kinetics. This analysis indicates on the possibility that the theory of thermally activated flow is exact enough to describe rate sensitivity of iron and mild steels up to strain rates of the order 10^5 to 10^6 s^{-1}, [53].

Another possibility, and more recent, to explain the pseudo-viscosity lies in the fact that some experimental data clearly indicate that the mechanical threshold $\hat{\tau}_0$ is itself rate sensitive, [54, 55]. Theoretical analyses of structural evolution which can lead to a rate sensitive mechanical threshold were also published recently, [56, 57].

An important observation, directly related to ASB in XC18 steel, are values of the critical total strain (elastic plus plastic) determined as a function of imposed velocity on MDS specimens. The final result is shown in Fig. 31 where the critical shear strains, $\Gamma_m = \delta_m/l_s$, are shown as a function of log $\dot{\Gamma}$. The mean values are shown as circles. The results for two lowest strain rates, $\dot{\Gamma} \approx 75$ s^{-1} and $\dot{\Gamma} \approx 750$ s^{-1}, were obtained with the loading rig and the fast closed-loop machine, the data for three highest strain rates in the range $1.8 \cdot 10^4$ s$^{-1} \leq \dot{\Gamma} \leq 4.7 \cdot 10^4$ s^{-1}, were obtained with the new experimental technique. The impact velocity at the highest nominal strain rate was ~ 100 m/s.

Since the dimensions of deforming parts of the MDS specimen are the same as the thickness of the layer studied by numerical methods, and the same steel was assumed for the numerical study, a direct comparison is possible between experimental results shown in Fig. 31 and numerical results of Fig. 3. Although values of localization strains are overall smaller than the critical strains found by experiment, at lower strain rates the same trend is observed, that is the total shear strain increases as a function of log $\dot{\Gamma}$. However, it is clear that at the highest strain rates an abrupt drop in the critical strain occurs. For example, the mean value of the critical strain from six tests

performed at $\dot{\Gamma} = 1.8 * 10^4$ s^{-1} (impact velocity ~ 30 m/s) is found $\Gamma_m \approx 2.60$, whereas the mean critical strain obtained from three tests at $\dot{\Gamma} = 4.7 * 10^4$ s^{-1} is $\Gamma_m \approx 0.85$. This result clearly indicates that the mechanism of the ASB's formation and propagation differs substantially at different initial and boundary conditions. In numerical calculations boundary conditions were the same, and were assumed as quasi-steady state of imposed velocity with a total absence of stress concentrators. in experiment the imposed velocity rises from zero by a projectile impact and stress concentrators are present as it is shown in Fig. 21, a and b. At lower rates the experimental mean values are perhaps higher in comparison to the numerical ones because a small additional displacement has occured due to some plastic deformation of the specimen supports.

A non-direct confirmation of reduction of the total shear strain at high impact velocity was attempted by the energy analysis. The total energy to fracture of all MDS specimens tested at high strain rates was determined and this result is shown in Fig. 32. Again, the energy drop is observed at the highest strain rate (impact velocity ~ 100 m/s). The drop is not too high in comparison to changes of the critical strain. mostly because of the positive strain rate sensitivity of flow stress.

A similar observation concerning energy consumption during fracturing of carbon steels by ASB formation was reported in [58]. Those results have been re-analysed by introduction of the mean strain rate and the final result is shown in Fig. 33 for 1010 and 1045 steels (German Standards Ck10 and Ck45). The so called "hat" specimen geometry was employed and specimens were deformed with SHPB at a narrow range of velocities, 5.5 m/s $\leq V_0 \leq 8.3$ m/s. Again. it is clear from Fig. 33 that the fracturing energy via formation and propagation of ASB's decreases for both steels when the nominal strain rate is increased. If the same logarithmic scale were applied in both figures (Fig. 32 and Fig. 33), a drop of fracturing energy would be very abrupt. A similar behavior, a decrease of fracture strain as a function of log $\dot{\Gamma}$, was found in [59] for 93% W alloy. This result is shown in Fig. 34. As before. for XC18 steel the critical fracturing strain diminishes abruptly around $\dot{\Gamma} = 10^4$ s^{-1}.

Those experimental results obtained for very high strain rates are in complete contradiction to the numerical predictions. for example Fig. 3. A further study is needed to clarify this discrepancy.

Fractographic study performed for XC18 steel by SEM revealed that for all velocities the fracture via ASB's occurs by creation and shearing of microvoids. No so called white bands were observed after perpendicular polishing and treatment by Nital. In some areas a very shiny patches were visible, those are the places where sliding of two neighbouring parts of the MDS specimen took place.

Four fractograms for MDS specimen deformed at impact velocity $V_0 = 100$ m/s are shown respectively in Figs. 35. 36. 37 and 38. Fig. 35 shows the boundary of the shiny surface and the dimpled region. Fig. 36 shows only the shiny part of the fracture surface with severe smeared deformation. Fig. 37 is the dimpled surface with some traces of cleavage. Finally, Fig. 38 shows a magnification of the dimpled region. Overall. a severe plastic deformation occurs locally near the fracture surface and some patches are deformed further due to local sliding. Temperature increase

in the local sliding areas must be quite high. This is supported by numerical results of Fig. 3. The local sliding and the mechanics of ASB's propagation should be studied further.

Experiments with VAR4340 steel

In order to study the impact velocity effects, or the nominal strain rate effects, on impact shearing, a series of tests have been performed with the Vacuum Arc Remelted AISI 4340 high strength steel. The original material was supplied by MTL-Watertown in the form of 305 x 305 x 9.52 mm cross rolled plates. The chemical composition of the supplied VAR4340 steel was as follows : C 0.42 ; Ni 1.74 ; Cr 0.89 ; Mn 0.46 ; Si 0.28 ; S 0.001 ; P 0.009 (% wt.). About forty MDS specimens were machined with geometry shown in Fig. 20b. The shear plane was assumed as perpendicular to the plane of the original cross rolled plate. After precision machining the MDS specimens were austenitized 1 hour at 925°C and oil quenched, re-austenitized 15 min at 845°C and oil quenched and finally tempered at 200°C during 2 hours. The final hardness was ~ 52 HRC. As it has been shown in [60] such thermal treatment assures maximum of the energy absorbed up to the point of instability at $\dot{\Gamma} = 10^5$ s^{-1}.

Around 30 MDS specimens were used for quasi-static and impact loading. In the case of loading at quasi-static rates the rig shown in Fig. 23 was used together with the closed-loop fast machine. In the case of impact loading four impact velocities were applied : $V_1 = 20$ m/s ; $V_2 = 35$ m/s ; $V_3 = 72$ m/s and $V_4 = 160$ m/s. For every nominal strain rate from three to five specimens were tested. At low strain rate, $\dot{\Gamma} = 1.1 * 10^4$ s^{-1}, some specimens fractured in the mixed mode, that is shearing and opening. The scanning electron micrography (SEM) of those surfaces revealed small facets of cleavage mixed with some ductile tearing. The cleavage facets showed a mean dia- meter of few micrometers. Diameters of plastic dimples were much smaller. At all higher rates, and also in some cases at this small strain rate, the fracturing occured in the shearing mode.

The level of shear strains to fracture was quite limited, for example at $\dot{\Gamma} = 1.1 * 10^{-4}$ s^{-1} the critical shear strain was around $\Gamma_{cr} = 0.0425$. The mean level of the maximum shear stress τ_m for MDS specimens tested at $\dot{\Gamma} = 1.1 * 10^{-4}$ s^{-1} was $\tau_m = 863$ MPa. For the same temper tested in torsion [61], HRC = 54, at $\dot{\Gamma} = 6 * 10^{-2}$ s^{-1} the maximum stress was $\tau_m = 1070$ MPa. It is found that relatively good agreement exists between data from a torsion test of a thin-walled specimen and the MDS test. Overall behavior of the critical shear stress as a function of log $\dot{\Gamma}$ is shown in Figs. 39a and b. The mean values of stress shown in Fig. 39b indicate for a maximum of τ_{cr} at $\dot{\Gamma} \sim 5 * 10^3$ s^{-1} and next a drop at higher strain rates occurs. The same experimental results are shown in the linear scale of $\dot{\Gamma}$ in Figs. 40a and b. Since the maximum impact velocity was $V_o = 160$ m/s, and at this velocity relatively small decrease of τ_{cr} was found, it is presumed that just beginning of a more severe drop of τ_{cr} was found. Thus, the critical impact velocity may be around 200 m/s with the nominal velocity of shearing $\dot{\Gamma}_{cr} = 10^5$ s^{-1}. Those values are higher in comparison to XC18

steel, Fig. 31. In certain regions of strain rate it is possible to calculate local strain rate sensitivities of the critical stress. This is demonstrated in Fig. 41 and Fig. 42 where by the broken lines the linear regions are indicated.

At low strain rates the standard rate sensitivity may be introduced β_F

$$\beta_F = \left(\frac{\partial \tau_c}{\partial \log \dot{\Gamma}} \right)_T \tag{63}$$

The slope indicated by the broken line gives $\beta_F = 54.79$ MPa.

At high strain rate region the linear rate sensitivity or pseudo-viscosity can be defined

$$\eta_F = \left(\frac{\partial \tau_c}{\partial \dot{\Gamma}} \right) \tag{64}$$

the slope of the broken line of Fig. 42 gives $\eta_F = 6.45$ Pa.s, value comparable to values for XC18 steel (Table 2).

A typical oscillogram for the MDS specimen of 4340 steel tested at $V_o = 160$ m/s shown in Fig. 13 indicates that the total energy to break the specimen is quite small as compared to XC18 steel which shows a large-strain plasticity. In the case of XC18 steel the peak of the total energy to break the MDS specimen can be estimated from Fig. 32 as $W = 230$ J, this number gives the energy absorbed per unit of shearing surface as $W/A = 2.4$ J/mm². An analysis of the total energy absorbed for three MDS specimens made of VAR4340 steel and loaded at impact velocity $V_o = 160$ m/s, give the mean value $W/A = 0.50$ J/mm². The total energy per unit area reported in [63] to break a thin-walled tubular specimen of VAR4340 steel, HRC40, at $\dot{\Gamma} = 10^3$ s⁻¹, was $W/A = 0.185$ J/mm². The mean energy absorbed up to the point of instability for "hat" specimens of VAR4340 steel, and for the same temper as in the present study, can be estimated from Fig. 7 of [60]. At an average displacement rate imposed on the "hat" specimen, $V = 5.1$ m/s, and at the local strain rate $\dot{\Gamma} = 10^5$ s⁻¹, the mean energy per unit area dissipated up to the maximum force is estimated as $W/A = 0.084$ J/mm².

Because of different specimen geometries and different imposed velocities, as well as thermal treatments, values of W/A for VAR4340 steel are not equal, but they give an order for this measure. Also, time to fracture were quite different at different experiments. For example, time to fracture in SHTB can be assumed as $t_f = 100$ μs, whereas time to fracture of the MDS specimen can be as short as several μs.

Since initial and boundary conditions play an important role in ASB's formation and fracturing, comparison of results from different experimental techniques must be studied further.

The next step in this study was fractographic examination of fracture surfaces by SEM. A review of previous metallographic and fractographic studies on surface morphologies after adiabatic shearing was given in [63]. In general, there is no agreement as to the occurence of phase

transformation in the so called "white bands". Recent studies seem to indicate that those bands consist of a very fine-grained, highly dislocated microstructure, [60]. The interior of so called "transformed" shear bands of 4340 steel showed an extremely fine microcrystalline structure with grain diameter ranging from 8 nm to 20 nm [60]. This observation supports the idea that no transformation occurs in the white bands and the interior of the band is a very heavily deformed martensite, [60]. The extremely fine graines are combined with the additional carbon in solution.

SEM micrography should provide further information on the separation mechanics of the white bands. Figures 43, 44, 45 and 46 show SEM pic: res of the same region of fractured surface of the MDS specimen deformed at impact velocity $V_o = 165.8$ m/s. The three typical morphologies of fracture surfaces can be observed in those figures. In Fig. 43, a small magnification, tongues of highly smeared material are identifiable. The borders of those tongues are marked by the brighter lines. The distances between the borders of tongues diminishes when the impact velocity is increased. In Fig. 44, a larger degree of magnification, the border of the smeared and dimpled zones are clearly visible. Fig. 45 shows the border between smeared and dimpled parts. The end of the tongue is covered with knobbles, which are characterized by spheroidized surface debris, apparently from a high temperature, close to the melting point [42]. This is probably a separated white band with a very fine microcrystalline structure, this microstructure is partially visible in the bottom of Fig. 45. The area in the upper side of the tongue, the same magnification as in Fig. 45, is shown in Fig. 46. This figure shows clearly identifiable elongated microvoids of diameter from 1 μm to 3 μm. The white spots visible in most of fractograms are probably debris of teflon dispersed after impact.

Another series of SEM micrograph examinations was performed for the MDS specimen loaded with the impact velocity $V_o = 71.9$ m/s. Again three typical morphologies of fracture surface can be identified. Fig. 47 shows the end of the tongue with the white border line. The magnified part of the border region is shown in Fig. 48. At the left bottom the tongue is covered with knobbles, at the right upper part the dimples are clearly visible. The central area of the tongue with the same magnification as the micrograph of Fig. 48 is shown in Fig. 49. This micrograph strongly indicates for an existence of a very high temperature in this region. The quasi-dimples are completely spheroidized and it indicates a viscous separation of surfaces.

The SEM examination of specimen surfaces produced at impact velocities 160 m/s and 72 m/s clearly revealed patches of elongated microvoids (Figs. 46 and 48). It is presumed that nucleation and coalescence of microvoids is the primary mechanism of the surface separation. Existence of tongues and knobbled surfaces indicate for an existence of high local temperature (close to the melting point) and severe sliding. Those regions may be much softer, and production of tongues can be explained by a local displacement of a soft material by sliding surfaces. When thickness of a sliding microlayer is sufficiently large a tongue is formed and the vicinities retain its dimpled structure. Separation of tongue regions occurs with presence of very high temperature, for example Fig. 49. Preliminary analyses indicate for an relation between the mean tongue size and velocity of

sliding. The proportion between knobbly and dimpled surfaces may depend on specimen geometry and loading conditions.

Present SEM fractographic study shows some similarities with results for VAR4340 steel (HRC40) reported in [63]. A further study is needed to define correlation between morphologies of micrographs and impact velocities.

Discussion and conclusions

This study has raised some points for further studies in the area of ASB's and fracture dynamics.

There is general agreement that the critical instability strain is related to the zero hardening condition. $d\tau/d\Gamma = 0$, of the adiabatic stress-strain curve. The post instability behavior is much more complex. In addition to material behavior. initial and boundary conditions could play decisive role in development and formation of ASB's and also fracture. The steady-state solutions, like the numerical one reported in this report, or analytical ones, are very useful tools in ASB studies, they can depict the late stage morphology during ASB development as a function of initial and boundary conditions. However. those solutions neglect stress concentrators which are always present in real situations including experiment. It has been shown in this study that the stress concentrators inverse the post localization behavior as a function of the nominal strain rate. To study further those effects a variety of experimental techniques must be applied with well specified initial and boundary conditions. The next inevitable step is a superposition of fracture dynamics on ASB morphology. Comparison of all available approaches for the same or similar materials may provide a data base on development and formation of ASB's.

It may be argued that in order to compare the susceptibility to adiabatic shear in different conditions. that is in presence of different stress concentrators, it is necessary to define the defect that initiates the localised ASB. It was suggested in [64] that the defect, or stress concentrator, must be scaled in an appropriate way to the homogeneous response in the onset of ASB.

The new experimental technique developed during this project permits for shear testing at large strains within a wide range of the nominal strain rates, from quasi-static up to 5×10^4 s^{-1}. The local strain rates during localization must be much higher. The configuration of impact experiment with MDS specimen and direct optical measurement of displacement permits for sufficient flexibility to change the notch geometry. The limiting case is to apply MDS specimen with symmetric fatigue cracks to study Mode II fracture under impact conditions. A general study of Mode II, quasi-static loading and dynamics, has been recently completed as the Appendix N° 1 to this Report, [4]. Dynamic plasticity has been included in this Mode II study. Also different notch geometries could be applied to vary stress concentrators.

The most important finding of this study is confirmation of the existence of the critical impact velocity in shear deformation. This velocity is around 100 m/s for the mild steel XC18 and above 160 m/s for VAR4340 steel (HRC 52). The experimental technique with MDS specimens permits for still higher impact velocities to be tested.

Another important area in studying ASB's is *post factum* metallographic examination of fracture surfaces. In the present study the SEM has been applied for both steels studied (XC18 and VAR4340 - HRC52). The mild steel XC18 showed large strains before the onset of instability. But those large strains were substantially reduced at impact velocity ~ 100 m/s. In the case of this steel a substantial adiabatic increase of temperature occurs not only during localization but before. On the contrary, in the case of VAR4340 the temperature increase prior to the onset of instability is not high, but during an abrupt localization the melting point can be reached in rubing islands, Fig. 49. The morphology of fracture and shearing velocity should be studied further, using perhaps an image analysis.

Although considerably more evidence must be gathered for other materials and other defect geometries, this study has revealed that the very important parameter in studying ASB's is the impact velocity.

Acknowledgements

References

[1] H. Tresca, On further applications of the flow of solids, *Proc. Inst. Mech. Engrs.* 30 (1878), 301.

[2] W. Johnson, Henri Tresca as the originator of adiabatic heat lines, *Int. J. Mech. Sci.* 29 (1987), 301.

[3] C. Zener and J.H. Hollomon, Effect of strain rate upon plastic flow of steel, *J. Appl. Phys.* 15 (1944), 22.

[4] I.V. Varfolomeyev and J.R. Klepaczko, Approximate analysis on strain rate effects and behavior of stress and strain fields at the crack tip in Mode II in metallic materials, Appendix N° 1 to the Technical Report submitted to the European Research Office, US Army RDSG, Con-

tract DAJA 45-90-C-0052 ; also Technical Reports ISGMP-LPMM, Metz University, (Oct. 1992).

[5] H.C. Rogers, Adiabatic plastic deformation, *Ann. Rev. Mater. Sci.* 9 (1979), 283.

[6] Y. Bai and B. Dodd, Adiabatic Shear Localization, Pergamon Press, Oxford (1992).

[7] C. Fressengeas, Analyse dynamique élasto-viscoplastique de l'hétérogénéité de la déformation plastique de cisaillement, *Proc. Int. Conf. on Mechanical and Physical Behaviour of Materials Under Dynamic Loading*, Les éditions de physique, Les Ulis (1988), C3-277.

[8] C. Fressengeas, Adiabatic shear morphology at very high strain rates, *Int. J. Impact Engng.* 8 (1989), 141.

[9] C. Fressengeas and A. Molinari, Non-linear approximate analysis of shear band formation, in : *Impact Loading and Dynamic Behaviour of Materials*, DGM Informationsgesellschaft Verlag, Oberursel, Vol. 2 (1988), 761.

[10] T.W. Wright, Approximate analysis for the formation of adiabatic shear bands, *J. Mech. Phys. Solids* 38 (1990), 515.

[11] L.S. Costin, E.E. Crisman, R.H. Hawley and J. Duffy, On the localization of plastic flow in mild steel tubes under dynamic torsional loading, in : *Proc. 2-nd Conf. on the Mechanical Properties of Materials at High Rates of Strain*, Inst. Phys. Conf. Ser. N° 47, Bristol (1979), 90.

[12] J.H. Giovanola, private communication (1989).

[13] A. Marchand and J. Duffy, An experimental study of the formation process of adiabatic shear bands in a structural steel, *J. Mech. Phys. Solids* 36 (1988), 251.

[14] Y.M. Leroy and A. Molinari, Stability of steady states in shear zones, *J. Mech. Phys. Solids* 40 (1992), 181.

[15] J. Litonski, Plastic flow of a tube under adiabatic torsion, *Bull. de l'Acad. Polonaise des Sciences*, série des Sciences Techniques XXV (1977), 7.

[16] J. Litonski, Numerical Analysis of Plastic Torsion Processes with Account on Heat Generated During Deformation, IFTR Reports, N° 33, Warsaw (19) ; (in Polish).

[17] M. Kaminski, Coupling of strain and temperature fields in the problem of torsion of a thin-walled tube, *Engineering Transactions* 24 (1976), 185 ; (in Polish).

[18] A.M. Merzer, Modelling of adiabatic shear band development from small imperfections, *J. Mech. Phys. Solids* 30 (1982), 323.

[19] S.L. Semiatin, M.R. Staker and J.J. Jonas, Plastic instability and flow localization in shear at high rates of deformation, *Acta Met.* 32 (1984), 1347.

[20] S.L. Semiatin, J.J. Jonas, T.G. Shawki and J. Duffy, Effect of material imperfections on flow localization in torsion, *Scripta Metall.* 21 (1987), 669.

[21] T.G. Shawki and R.J. Clifton, Shear band formation in thermal viscoplastic materials, *Mech. of Materials* 8 (1989), 13.

[22] T.J. Burns, A mechanism of shear band formation in the high strain-rate torsion test, *J. Appl. Mech.* 57 (1990), 836.

[23] O. Oussouaddi and J.R. Klepaczko, An analysis of transition between isothermal and adiabatic deformation for the case of torsion of a tube, in : *Proc. 3rd International Conference on Mechanical and Physical Behaviour of Materials under Dynamic Loading*, Les éditions de physique, Les Ulis (1991), C3-323.

[24] Z. Marcinak and K. Kuczynski, Limit strains in the process of stretch-forming sheet metal, *Int. J. Mech. Sci.* 9 (1967), 609.

[25] R. Dormeval, Adiabatic shear phenomenon, in : *Materials at High Strain Rates*, Elsevier Appl. Sci., London (1987), 47.

[26] J.R. Klepaczko, Adiabatic shear bands, review of experimental techniques and results, in : *Mécanique, Modélisation Numérique et Dynamique des Matériaux*, Publications LMA-CNRS N° 124, Marseille (1991), 335.

[27] A. Molinari and R.J. Clifton, Localisation de la déformation viscoplastique en cisaillement simple : résultats exacts en théorie non linéaire, *C.R. de l'Acad. Sci., Ser. II*, 296 (1983), 1.

[28] M.V. Buisson and A. Molinari, Bandes de cisaillement stationnaires dans un acier, in : Proc. Int. Conf. on Mechanical and Physical Behaviour of Materials Under Dynamic Loading, Les éditions de physique, Les Ulis (1988), C3-167 ; (in French).

[29] K.A. Hartley, J. Duffy and R.H. Hawley, Measurement of the temperature profile during shear band formation in steels deforming at high strain rates, *J. Mech. Phys. Solids* 35 (1987), 283.

[30] G.R. Johnson, Dynamic analysis of a torsion test specimen including heat conduction and plastic flow, *J. Engng. Materials and Technol.* 103 (1981), 201.

[31] J.R. Klepaczko, The Relation of Thermally Activated Flow in BCC Metals and Ferritic Steels to Strain Rate History and Temperature History Effects, Technical Report DMR-79-23257/2, Materials Research Laboratory, Brown University, Providence (1981).

[32] J.R. Klepaczko, P. Lipinski and A. Molinari, An analysis of the thermoplastic catastrophic shear in some metals, in : *Impact Loading and Dynamic Behavior of Materials*, DGM Informationsgesellschaft Verlag, Oberursel, Vol. 2 (1988), 695.

[33] J.R. Klepaczko, A practical stress-strain-strain rate-temperature constitutive relation of the power form, *J. Mech. Working Technology* 15 (1987), 143.

[34] T.W. Wright and J.W. Walter, On stress collapse in adiabatic shear bands, *J. Mech. Phys. Solids* 35 (1987), 701.

[35] T.W. Wright and J.W. Walter, Adiabatic shear bands in one dimension, in : *Mechanical Properties of Materials at High Rates of Strain 1989*, Inst. Phys. Conf. Ser. N° 102, Bristol (1989), 119.

[36] J.R. Klepaczko and B. Rezaig, A numerical study of rate effects in shear band formation ; in preparation.

[37] J.R. Klepaczko, Modelling of structural evolution at medium and high strain rates, FCC and BCC metals, in : *Constitutive Relations and Their Physical Basis*, Risö Natl. Laboratory, Roskilde, Danemark (1987), 387.

[38] J.R. Klepaczko, A general approach to rate sensitivity and constitutive modelling of FCC and BCC metals, in : *Impact : Effects of Fast Transient Loadings*, A.A. Balkema, Rotterdam (1988), 3.

[39] N.E. Zeghib, Experimental study and Modeling of Plastic Deformation with Dynamic Strain Ageing, Case of Mild Steels, Ph. D. Thesis, Metz University, ISGMP-LPMM, Metz (1990).

[40] U.F. Kocks, A.S. Argon and M.F. Ashby, *Thermodynamics and Kinetics of Slip*, Pergamon Press, Oxford (1976).

[41] J.R. Klepaczko, A Model for Yielding and Flow of Iron and BCC Metals Based on Thermal Activation, Technical Report DMR-79-2325/132, Brown University, Providence (1981).

[42] D.D. Makel and G.F. Wilsdorf, Localized melting during the separation of high strength tensile sampies, in : *Shock-Wave and High-Strain-Rate Phenomena in Materials*, Marcel Dekker, Inc., New York (1992), 693.

[43] J.R. Klepaczko, An experimental technique for shear testing at high and very high strain rates, case of a mild steel, *Int. J. Impact Engng.*, (accepted).

[44] K.F. Graff, Wave Motion in Elastic Solids, Oxford University Press, Oxford (1975).

[45] R. Folk, G. Fox, C.A. Shook and C.W. Curtis, Elastic strain produced by sudden application of pressure to one end of a cylindrical bar : 1. Theory, *J. Acoust. Soc. Amer.* 30 (1958), 552.

[46] R. Skalak, Longitudinal impact of a semi-infinite circular elastic bar, *J. Appl. Mech.* 24 (1957), 59.

[47] J.R. Klepaczko and S.J. Matysiak, Analysis of Longitudinal Impact on Semi-infinite Circular Bars and Tubes, Appendix N° 2 to the Final Technical Report, Contract DAJA 45-90-C-0052. (October 1992).

[48] J.D. Campbell and W.G. Ferguson, The Temperature and strain-rate dependence of the shear strength of mild steel, *Phil. Mag.* 21 (1970), 63.

[49] W.G. Ferguson, F.E. Hauser and J.E. Dorn, Dislocation damping in zinc single crystals, *Brit. J. Appl. Phys.* 18 (1967), 411.

[50] J.R. Klepaczko, The strain rate behavior of iron in pure shear, *Int. J. Solids Struct.* 5 (1969), 533.

[51] R.W. Klopp and R.J. Clifton, Pressure-Shear Impact and the Dynamic Viscoplastic Response of Metals, Workshop Proc. on *Inelastic Deformation and Failure Modes*, Northwestern University, USA, (Nov. 1989).

[52] H. Conrad, Thermally activated deformation in metals, *J. of Metals* 16 (1969), 582.

[53] T. Nojima, Constitutive equation of some kinds of steel at high rates of strain, *Impact Loading and Dynamic Behaviour of Materials*, Vol. 1, DGM-Informationsgesellschaft Verlag, Oberursel, FRD (1988), 357.

[54] P.S. Follansbee, The rate dependence of structure evolution in copper and its influence on the stress-strain behavior at very high strain rates, *Impact Loading and Dynamic Behavior of Materials*, Vol. 1, DGM-Informationsgesellschaft Verlag, Oberursel, FRG (1988), 315.

[55] S. Tanimura, T. Hayashi and K. Ishikawa, Strain rate and temperature effects on the strength of high strength materials, *Microstructure and Mechanical Behaviour of Materials*, Vol. II, EMAS, Warley, UK (1985), 761.

[56] J.R. Klepaczko, On modeling of structural evolution in metals at different strain rates and temperatures, *Inelastic Solids and Structures*, Pineridge Press, Swansea, UK (1990), 179.

[57] J.R. Klepaczko, The newest development on physically based constitutive modeling in dynamic plasticity, Proc. ICM6, *Mechanical Behaviour of Materials-VI*, Vol. 1, Pergamon Press, Oxford (1991), 235.

[58] T. Pintat, B. Scholz, H.D. Kunze and O. Vöhringer, The influence of carbon content and grain size on energy consumption during adiabatic shearing, in : *Proc. Int. Conf. on Mechanical and Physical Behaviour of Materials Under Dynamic Loading*, Les éditions de physique, Les Ulis (1988), C3-237.

[59] T. Weerasooriya, P.A. Beaulieu and R. Swanson, Deformation and Failure of 93W-5Ni-2Fe at High Strain Rate Shear Loading, Technical Report MTL TR 92-19, Watertown, MA (1992).

[60] J.H. Beatty, L.W. Meyer, M.A. Meyers and S. Nemat-Nasser, Formation of Controlled Adiabatic Shear Bands in AISI 4340 High Strength Steel, Technical Report MTL TR 90-54, Watertown, MA (1990).

[61] S. Tanimura and J. Duffy, Strain Rate Effects and Temperature History Effects for Three Different Tempers of 4340 VAR Steels, Technical Report N° DAAG 29-81-K-0121/4, Brown University, Providence (1984).

[62] J.H. Giovanola, Adiabatic shear banding under pure shear loading, Part I : Direct observation of strain localization and energy dissipation measurements, *Mech. of Materials* 7 (1988), 59.

[63] J.H. Giovanola, Adiabatic shear banding under pure shear loading, Part II : Fractographic and metallographic observations, *Mech. of Materials* 7 (1988), 73.

[64] T.W. Wright, Shear band susceptibility : work hardening materials, *Int. J. Plast.* 9 (1993), (to appear).

Figures

Fig. 1   a. Gradient of temperature ($\partial T/\partial x$) as a function of log $\dot{\Gamma}_n$ for L = 2.0 mm ; 1-mild steel, 2-aluminum, 3-copper ;

b. Values of ξ as a function of log $\dot{\Gamma}_n$; L = 2.0 m, maximum of ξ defines transition $(\dot{\Gamma}_n)_{cr}$.

Fig. 2   Critical values of shear strain rates $(\dot{\Gamma}_n)_{cr}$ as a function of tube length L ; + - copper, * - aluminum, o - steel.

Fig. 3   Nominal values of instability strain Γ_c and localization strain Γ_{LOC} as a function of the nominal strain rate $\dot{\Gamma}_n$ = V/h, numerical simulation for XC18 steel.

Fig. 4   Nominal values of instability strain Γ_c in expanded scale as a function of the nominal strain rate $\dot{\Gamma}_n$, numerical simulation for XC18 steel.

Fig. 5   The ratio of Γ_c/Γ_{LOC} as a function of log $\dot{\Gamma}_n$, numerical simulation for XC18 steel.

Fig. 6   Localization of shear strain at different levels of the nominal strain Γ_n at $\dot{\Gamma}_n = 10^3$ s^{-1}.

Fig. 7   Localization of temperature at different levels of the nominal strain Γ_n at $\dot{\Gamma}_n = 10^3$ s^{-1}.

Fig. 8   Evolution of strain gradients g_Γ (y) at the same levels of the nominal strain as indicated in Fig. 6, nominal strain rate $\dot{\Gamma}_n = 10^3$ s^{-1}.

Fig. 9   Evolution of strain gradients in the half-thickness of the layer at $\dot{\Gamma}_n = 10^3$ s^{-1} and different levels of nominal strain Γ_n ; dashed line shows the asymptotic procedure in finding the ASB thic ness.

Fig. 10   Evolution of the ASB band thickness as a function of the nominal strain rate : o - analysis based on strain gradients ; * - analysis based on temperature gradients.

Fig. 11   New configuration of experimental setup developed in LPMM-Metz : P - projectile : S - double shear specimen : L - source of light : 1,2,3 - fiber optics : F - photodiodes : TC1, TC2 - time counters : E - optical extensometer : T$_1$ - strain resistance gage : S - DC supply unit : A1 - amplifier : DO - digital oscilloscope : PC - personal computer : R - XY recorder or graphic printer.

Fig. 12   Oscillogram from the test of XC18 steel at impact velocity V_o = 35.08 m/s : upper trace is the signal from SR station T1 : lower trace is the displacement signal from the optical extensometer.

Fig. 13   Oscillogram from the test of VAR 4340 steel at impact velocity V_o = 160 m/s : the upper trace is the signal from SR station T1, the lower trace is the displacement signal from the optical extensometer.

Fig. 14   Details of the Hopkinson tube :

a. the face at which pressure is applied - shadowed surface supports MDS specimen (a x b) :

b. dimensions and distances used in FE calculations x_1 = 90.5 mm ; x_2 = 170.5 mm.

Fig. 15 Initial conditions of pressure on the surface 2 (a x b) as shown in Fig. 14 ; trapezoid pulses with different times t_r, t_o and t_a as shown at the bottom.

Fig. 16 Results of FE calculations ε (t) for x_1 = 90.5 mm, case N° 1 of Fig. 14, solid and bro ken lines are respectively for external and internal surface of the tube ; a - plane parallel to the MDS specimen ; b - perpendicular plane.

Fig. 17 Results of FE calculations ε (t) for x_2 = 170.5 mm, case N° 1 of Fig. 14, solid and bro- ken lines are respectively for external and internal surface of the tube ; a - plane parallel to the MDS specimen ; b - perpendicular case.

Fig. 18 Results of FE calculations ε (t) for x_1 = 90.5 mm, case N° 4 of Fig. 14.

Fig. 19 Results of FE calculations ε (t) for x_2 = 170.5 mm, case N° 4 of Fig. 14.

Fig. 20 Two specimens with modified geometries for double shear tests ; a - geometry initially assumed after modifications with respect to [48] ; b - perfected geometry with enlarged supports.

Fig. 21 Distribution of shear stresses in MDS specimen after nominal shear strain : (a) Γ = 2.5 x 10^{-3} ; (b) Γ = 0.50.

Fig. 22 Distribution of the shear strain component in MDS specimen after nominal shear strain : (a) Γ = 2.5 x 10^{-3} ; (b) Γ = 0.50.

Fig. 23 Rig for deformation of MDS specimens at different strain rates, from 10^{-4} s^{-1} to 10^3 s^{-1}, using a fast closed-loop testing machine ; MDS specimen is shadowed.

Fig. 24 Values of the nominal shear strain rate $\dot{\Gamma}$ as a function of gage length l_s for two axial velocities V_o 20 m/s and 1 0 m/s ; CF - gage lengths used in [48] ; JRK - gage length l_s = 2.0 mm used in MDS specimen.

Fig. 25 Variation of upper yield stress τ_y in shear with logarithm of strain rate, log $\dot{\Gamma}$, MDS spe- cimen.

Fig. 26 Upper yield stress τ_y versus shear strain rate $\dot{\Gamma}$ in linear scale of $\dot{\Gamma}$.

Fig. 27 Variation of lower yield stress τ_{yl} in shear with logarithm of shear strain rate, log $\dot{\Gamma}$; ■ - MDS specimen ; + - experimental points from ref. [48].

Fig. 28 Comparison of results for lower yield stress τ_{yl} for XC18 steel of Modified Double shear (■), and inclined impact (o) for pure iron. [15].

Fig. 29 Upper yield stress τ_y versus shear strain rate $\dot{\Gamma}$ in linear scale, XC18 steel, MDS speci- men ; broken line shows the best linear fit.

Fig. 30 Lower yield stress τ_{yl} versus shear strain rate $\dot{\Gamma}$ in linear scale ; XC18 steel, MDS speci- men ; broken line shows the best linear fit.

Fig. 31 Shear strains of localization versus log $\dot{\Gamma}$; XC18 steel, MDS specimen ; circles denote mean values.

Fig. 1

b.

VARIATION (dT/dx)

0.950E+04
0.760E+04
0.570E+04
0.380E+04
0.190E+04
0.000E+00

0.00   0.50   1.00   1.50   2.00   2.50   3.00

LOG $\hat{I}^c$

L = 2.0 mm

a.

TEMPERATURE GRADIENT dT/dx

0.450E+04
0.360E+04
0.270E+04
0.180E+04
0.900E+03
0.000E+00

0.00   0.50   1.00   1.50   2.00   2.50   3.00

LOG $\hat{I}^c$

L = 2.0 mm

Fig. 2

Fig.3

Fig. 4

Fig. 5

$\Gamma = .33\ .37\ .41\ .45\ .49\ .51\ .54\ .57\ .61$

$\Gamma = .61$

$\Gamma = .33$

$\dot{\Gamma} = 1000\ s-1$

Y(mm)

Fig. 4

Temperature [K]

$\Gamma = .33\ .37\ .41\ .45\ .49\ .51\ .54\ .57\ .61$

$\Gamma = .61$

$\Gamma = .33$

$\dot{\Gamma} = 1000\ s-1$

$d\Gamma/dY$

$1.4E+04$

$1.2E+04$

$1.0E+04$

$8.0E+03$

$6.0E+03$

$4.0E+03$

$2.0E+00$

$0.0E+00$

0 0.2 0.4 0.6 0.8 1 1.2 1.4 1.6 1.8 2

$Y(mm)$

Fig. 9

$d\Gamma/$

$1.4E+04$ $\Gamma = .33$ $.37$ $.41$ $.45$ $.49$ $.51$ $.54$ $.57$ $.61$

$1.2E+04$ $\Gamma = 61$

$1.0E+04$

$\Gamma = .33$

$8.0E+03$

$6.0E+03$

$4.0E+03$

$\dot{\Gamma} = 1000\ s-1$

$2.0E+03$

$0.0E+00$

0 0.2 0.4 0.6 0.8 1

$Y(mm)$

Fig. 10

Fig. 11

```
-50.0000 us            160.000 us            410.000 us
                       50.0 us/div                realtime

Vmarker2( 2 )    145.750mv      stop marker:   294.000us
Vmarker1( 2 )   -745.750mv      start marker:   31.0000us
delta V( 2 )     997.500mv          delta t:   263.000us
                                  1/delta t:    3.8023kHz
```

Fig. 12

```
TIMEBASE
         20.0 us/div
       50.0 us/div
   delay
         -20.0000 us
       -100.000 us
   reference
  left  main  right
```

```
-120.000 us            -20.0000 us            30.0000 us
                       20.0 us/div                realtime

Vmarker2( 2 )   -23.0959mv      stop marker:  -17.2000us
Vmarker1( 2 )   -1.77947 V      start marker: -37.2000us
delta V( 2 )     1.75137 V          delta t:   20.0000us
                                  1/delta t:   50.0000kHz
```

```
repetitive
equivalent
```

fine

```
           Sensitivity    Offset        Probe     Coupling    Impedance
Channel 1  200  mV/div  -300.000 mV      1:1      ac LF rej    1M ohm
Channel 2  300  mV/div  -1.10514  V    0.999:1      dc         1M ohm
```

Fig. 13

a)

b)

Fig. 14

INITIAL CONDITIONS AT THE END OF TUBE
(TRAPEZOID PULSE)
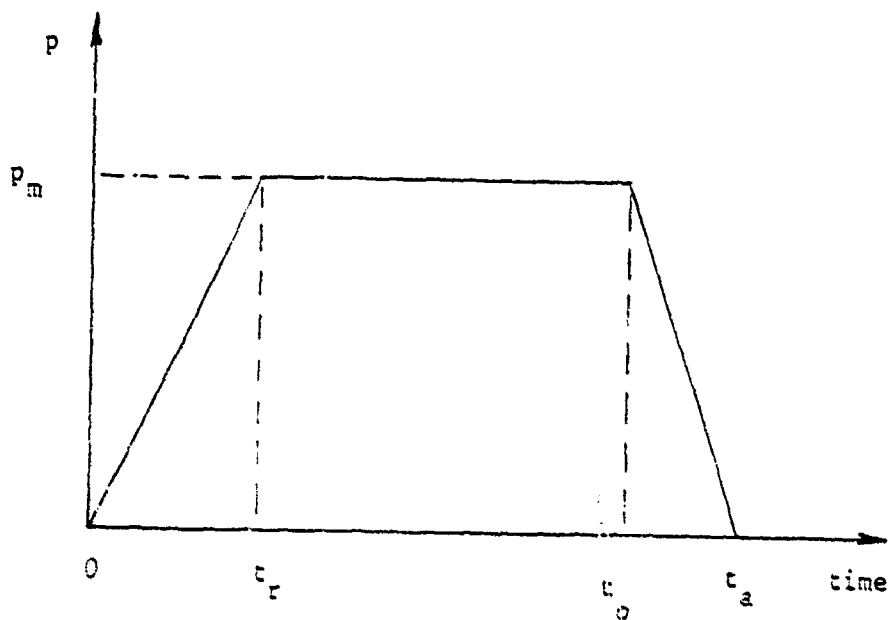
CALCULATED CASES

N°	P_m (MPa)	t_r (μs)	t_o (μs)	t_a (μs)
1	450	20	10	20
2	450	20	20	20
3	450	10	10	10
4	450	5	5	5
5	300	20	160	20
6	300	10	20	20
7	150	20	160	20
8	150	20	20	20

Fig. 15

Tube

Section at 90.5 mm. in the axis of impact

a)

$t_s=20$ μs
$t_b=10$ μs
$t_a=20$ μs

$p_{max}=450$ MPa

external surface
internal surface

Tube

Section at 90.5 mm. 90° from the axis of impact

b)

$t_s=20$ us
$t_b=10$ us
$t_a=20$ us

$p_{max}=450$ MPa

external surface
internal surface

Tube

Section at 170.5 mm, in the axis of impact

a)

t_s=20 µs
t_0=10 µs
t_s=20 µs

p_{max}=450 MPa

— external surface
.... internal surface

Tube

Section at 170.5 mm, 90° from the axis of impact

b)

t_s=20 µs
t_0=10 µs
t_s=20 µs

p_{max}=450 MPa

— external surface
.... internal surface

Tube

Section at 90.5 mm, in the axis of impact

a)

t_r=5 µs
t_0=5 µs
t_s=5 µs

p_{max}=450 MPa

Longitudinal strain

Time [µs]

— external surface
...... internal surface

Tube

Section at 90.5 mm, 90° from the axis of impact

b)

t_r=5 µs
t_0=5 µs
t_s=5 µs

p_{max}=450 MPa

Longitudinal strain

Time [µs]

— external surface
— internal surface

Tube

Section at 170.5 mm, in the axis of impact

a)

$t_r = 5\ \mu s$
$t_0 = 5\ \mu s$
$t_a = 5\ \mu s$

$p_{max} = 450$ MPa

Tube

Section at 170.5 mm, 90° from the axis of impact

b)

$t = 5\ \mu s$
$t_r = 5\ \mu s$
$t_a = 5\ \mu s$

$p_{max} = 450$ MPa

Fig. 19

a)

b)

Fig. 20

a)

b)

Fig. 21

a)

b)

Fig. 22

Fig. 23.

Fig. 24

STEEL XC18

UPPER YIELD POINT

SHEAR STRESS [GPa]

LOG STR.RATE [s-1]

Fig. 25

STEEL XC18

UPPER YIELD POINT

SHEAR STRESS [GPa]

STR.RATE [s-1*1E4]

Fig. 26

Fig. 27

Fig. 20

STEEL XC18

LOWER YIELD STRESS

STEEL XC18

UPPER YIELD POINT

STEEL XC18

CRITICAL SHEAR STRAIN

Fig. 31

Fig. 32

Fig. 33

Fig. 34

Voyager Image Display

x: y: i: Grey1:xc122

|— 200 um —|

Fig. 35

Voyager Image Display

x: y: t: Grey1:FDGHDJ

|← 200 um →|

Fig. 36

Voyager Image Display

x: y: r: Grey1:xc121

|← 40 um →|

Fig. 37

Fig. 28

a) STEEL VAR4340

b) STEEL VAR4340 — MEAN VALUES

Fig. 39

STEEL VAR4340

a)

MEAN VALUES

STEEL VAR4340

b)

Fig. 40

Fig. 41

Voyager Image Display

x: y: r: Grey1:vcv.121

|←   120   um   →

Fig. 43

Fig. 44

Fig. 83

Grey1 : vdv.12.1

FIG. 4

Voyager Image Display

x:50   y:50   i:60   Grey1

30 um

Fig. 47

Voyager Image Display

6 um

Fig. 48

Fig. 49